The Astrophysical Journal, 946:106 (24pp), 2023 April 1 https://doi.org/10.3847/1538-4357/acb0c4
© 2023. The Author(s). Published by the American Astronomical Society.
OPEN ACCESS

Magnetic Misalignment of Interstellar Dust Filaments

Ari J. Cukierman[1,2,3], S. E. Clark[1,2], and George Halal[1]
[1] Department of Physics, Stanford University, Stanford, CA 94305, USA; ajcukier@caltech.edu
[2] Kavli Institute for Particle Astrophysics and Cosmology, SLAC National Accelerator Laboratory, 2575 Sand Hill Road, Menlo Park, CA 94025, USA
[3] Department of Physics, California Institute of Technology, Pasadena, CA 91125, USA
Received 2022 August 23; revised 2022 December 22; accepted 2023 January 4; published 2023 April 5

Abstract

We present evidence for scale-independent misalignment of interstellar dust filaments and magnetic fields. We estimate the misalignment by comparing millimeter-wave dust-polarization measurements from Planck with filamentary structures identified in neutral-hydrogen (H I) measurements from HI4PI. We find that the misalignment angle displays a scale independence (harmonic coherence) for features larger than the HI4PI beamwidth (16.′2). We additionally find a spatial coherence on angular scales of $\mathcal{O}(1^\circ)$. We present several misalignment estimators formed from the auto- and cross-spectra of dust-polarization and H I-based maps, and we also introduce a map-space estimator. Applied to large regions of the high-Galactic-latitude sky, we find a global misalignment angle of $\sim 2^\circ$, which is robust to a variety of masking choices. By dividing the sky into small regions, we show that the misalignment angle correlates with the parity-violating *TB* cross-spectrum measured in the Planck dust maps. The misalignment paradigm also predicts a dust *EB* signal, which is of relevance in the search for cosmic birefringence but as yet undetected; the measurements of *EB* are noisier than those of *TB*, and our correlations of *EB* with misalignment angle are found to be weaker and less robust to masking choices. We also introduce an H I-based dust-polarization template constructed from the Hessian matrix of the H I intensity, which is found to correlate more strongly than previous templates with Planck dust *B* modes.

Unified Astronomy Thesaurus concepts: Interstellar medium (847); Interstellar filaments (842); Interstellar magnetic fields (845); Interstellar atomic gas (833); Neutral hydrogen clouds (1099); Magnetic fields (994); Astrophysical magnetism (102); Milky Way magnetic fields (1057); Cosmic microwave background radiation (322); Cosmology (343); Interstellar dust (836); Dust continuum emission (412)

1. Motivation

We continue the investigation of magnetic misalignment from Clark et al. (2021), who sought an explanation for the parity-violating *TB* correlation measured in Galactic dust polarization by the Planck satellite at millimeter wavelengths (Planck Collaboration et al. 2020a). A polarization field can be generically decomposed into parity-even *E* modes and parity-odd *B* modes (Kamionkowski et al. 1997; Seljak & Zaldarriaga 1997). The *TB* cross-spectrum is a measure of the correlation between the total intensity *T* and the *B*-mode polarization and indicates a net chirality in the polarization field. The *TE* cross-spectrum is a correlation with the *E*-mode polarization and is nonchiral. Using the dust-dominated frequency channel centered at 353 GHz, Planck Collaboration et al. (2020a) reported $TB/TE \sim 0.1$ in the multipole range $40 < \ell < 600$, which roughly corresponds to angular scales of 1°–10°.

Parity-probing cross-spectra such as *TB* and *TE* are of interest both in studies of the interstellar medium (ISM), for which the observed cross-spectra may constrain magnetohydrodynamic (MHD) models (Caldwell et al. 2017; Kandel et al. 2017; Kritsuk et al. 2018; Kim et al. 2019), and in measurements of the cosmic microwave background (CMB), for which asymmetries in the Galactic foregrounds can bias polarization calibration (Abitbol et al. 2016) and confound searches for cosmic birefringence (Minami & Komatsu 2020). A magnetic helicity in the local ISM (Brandenburg & Subramanian 2005; Blackman 2015) could produce a nonzero *TB* correlation, and Bracco et al. (2019) produced toy models with positive *TB* and *TE* on large scales (multipoles $\ell \lesssim 20$).

The polarization of interstellar dust emission is a probe of Galactic magnetic fields, the observed polarization orientation being perpendicular to the plane-of-sky (POS) magnetic field (Stein 1966; Hildebrand 1988; Martin 2007). At the same time, the dust in the diffuse ISM is partially organized in filamentary structures that are preferentially aligned to the magnetic field (Planck Collaboration et al. 2016a, 2016b). Filamentary structures can also be identified in neutral hydrogen (H I), which is well mixed with dust (Lenz et al. 2017) and has the advantage of three-dimensional information from spectroscopic separation into velocity bins. The alignment between H I filaments and magnetic-field orientations has been confirmed by comparison to millimeter-wave and optical-starlight polarization (McClure-Griffiths et al. 2006; Clark et al. 2014, 2015; Martin et al. 2015; Kalberla et al. 2016).

Whereas previous work, e.g., Clark & Hensley (2019), assumed a perfect alignment between interstellar dust filaments and magnetic-field lines, it was suggested in Huffenberger et al. (2020) that a small misalignment could act as a mechanism for parity violation, i.e., a tendency toward features of one chirality (or handedness) over the other. In Clark et al. (2021), this idea was extended to allow dust filaments and magnetic-field orientations to display a scale-dependent misalignment, which could potentially account for the observed *TB*.

In this work, we directly compute the misalignment angle in many regions of the sky and many multipole bins for $\ell > 100$. We find evidence for scale independence of the misalignment angle and also for a correlation with the observed dust *TB*.

Original content from this work may be used under the terms of the Creative Commons Attribution 4.0 licence. Any further distribution of this work must maintain attribution to the author(s) and the title of the work, journal citation and DOI.

1.1. *Observed* TB

The dust *TB* was reported in Planck Collaboration et al. (2016c), where it was noted that a positive signal in the multipole range $60 < \ell < 130$ became more significant as the sky area was increased. The investigation was continued in Planck Collaboration et al. (2020a) with the observation that $TB/TE \sim 0.1$ for $40 < \ell < 600$. The *EB* signal was reported to be consistent with null.

In Weiland et al. (2020), the *TB* signal was further confirmed by using Wilkinson Microwave Anisotropy Probe (WMAP) *K*-band polarization (Page et al. 2007) in place of the Planck *B* modes and also by using the magnetic-field template from Page et al. (2007) that is based on optical starlight-polarization catalogs (Heiles 2000; Berdyugin et al. 2001, 2004; Berdyugin & Teerikorpi 2002). The *K*-band measurement is dominated by synchrotron rather than dust emission but is also a probe of Galactic magnetic fields. The starlight measurements largely probe the same magnetic dust-grain alignment that produces polarized millimeter-wave emission. Both choices are independent of the Planck polarization calibration, and both show positive *TB*.

1.2. Magnetic Misalignment

Magnetic misalignment is a discrepancy between the orientation of filamentary density structures and the polarization-inferred magnetic-field lines. In the case of perfect magnetic alignment, we expect $TE > 0$ and $TB = 0$ (Zaldarriaga 2001). A misalignment of 45° would produce $TE = 0$ and $TB \neq 0$, where the sign depends on the chirality of the misalignment. The robustly positive *TE* measured by Planck can be interpreted as supportive evidence for magnetic alignment of dust filaments (Clark et al. 2015; Planck Collaboration et al. 2016b; Kalberla et al. 2016). In Planck Collaboration et al. (2020a), the *TE* correlation over sky regions and multipoles is reported as $r_\ell^{TE} = D_\ell^{TE}/\sqrt{D_\ell^{TT} D_\ell^{EE}} = 0.357 \pm 0.003$, where D_ℓ^{XY} denotes the cross-spectrum of *X* and *Y*; the *TB* correlation is reported as $r_\ell^{TB} = D_\ell^{TB}/\sqrt{D_\ell^{TT} D_\ell^{BB}} \approx 0.05$. Since the *TB* correlation is much smaller than the *TE* correlation, the magnetically aligned model need only be perturbed a small but coherent amount in order to produce the observed *TB*, and this perturbation would also produce a positive *EB* (Huffenberger et al. 2020), though this *EB* would be obscured by Planck noise (Clark et al. 2021).

In Clark et al. (2021), it was suggested that an H I-based filamentary polarization template could be used as a comparison point in the search for magnetic misalignment. The template of Clark & Hensley (2019) is constructed by (1) quantifying the orientation of linear H I structures with the rolling Hough transform (RHT; Clark et al. 2014) in velocity-channel maps from HI4PI (HI4PI Collaboration et al. 2016), (2) assuming perfect alignment between the RHT-measured H I orientation and the POS magnetic-field orientation and thereby obtaining a prediction for the dust polarization angle, (3) applying weights based on the H I intensity, and (4) integrating the channel maps to form a template that can be compared to the measured millimeter-wave dust polarization. A strong correlation with the Planck 353 GHz maps is detected in both *E* and *B* modes up to the HI4PI beam scale of 16.′2 ($\ell \lesssim 1000$). The HI4PI-based template was used in Clark et al. (2021), but Clark & Hensley (2019) also constructed polarization templates with observations from the Galactic Arecibo L-Band Feed Array H I Survey (Peek et al. 2018), which has higher angular resolution (FWHM = 4.′1) but smaller sky coverage (32% of the celestial sphere).

Given the alignment between H I and dust filaments, a difference between the Planck-measured dust polarization angles and the H I-inferred angles is a potential indication of magnetic misalignment and could be used as a tracer of dust *TB* and *EB* (Clark et al. 2021). In extending the work of Clark et al. (2021), we measure the aggregate misalignment angle in different sky regions by using the H I template as a reference. We study the observed properties of this misalignment angle and its correlation with the measured dust *TB* and *EB*.

Clark et al. (2021) also introduced a scale-dependent effective misalignment angle ψ_ℓ, which is a function of multipole ℓ. This effective misalignment angle is given explicitly by (cf. Equation (11) of Clark et al. 2021)

$$\psi_\ell \equiv \frac{1}{2} \arctan \frac{D_\ell^{TB}}{D_\ell^{TE}}, \tag{1}$$

where we see that the ratio TB/TE is the controlling quantity.[4] As noted in Planck Collaboration et al. (2020a), the ratio TB/TE is approximately constant across a broad range of multipoles at high Galactic latitudes, and this is related to the observation of Clark et al. (2021) that $\psi_\ell \sim 5°$ in the range $100 \lesssim \ell \lesssim 500$ on a similar sky area.

Equation (1) provides an estimator for the effective misalignment angle. Because it is formed from the *TB* and *TE* cross-spectra, we will call this type of estimator "spectrum-based." In this work, we present several additional spectrum-based estimators by considering the auto- and cross-spectra of the Planck dust maps and H I templates. We also present a map-based estimator that is similar to the projected Rayleigh statistic of Jow et al. (2017). We test for consistency among these estimators.

Although Clark et al. (2021) allowed for scale dependence in the misalignment angle, we find in this work that ψ_ℓ tends to display a scale independence even when measured on small regions of the sky. Equivalently, we find that ψ_ℓ is roughly constant with ℓ, which we will occasionally refer to as "harmonic coherence."

It is important to note that the dust is likely organized only partially in filaments, which are in turn only partially captured by the H I template. We expect, therefore, that there are contributions to the dust polarization that are unrelated to the H I template and, more generally, unrelated even to the true underlying filamentary structure. An estimator like that of Equation (1) may be influenced by these nonfilamentary contributions, since it depends only on the *TB* and *TE* cross-spectra of the full dust maps. Some of the estimators we will introduce in later sections will be defined by reference to the H I template, which will partially but imperfectly restrict the analysis to modes that are related to filaments.

In contrast to the previous paragraph, the `DUSTFILAMENTS` code of Hervias-Caimapo & Huffenberger (2022) constructs a phenomenological dust model, which is composed entirely of filaments and reproduces the main features of the angular power spectra measured by Planck. Using this model, it was recently shown in Huang (2022) that the measured *TB* is

[4] We use the notation D_ℓ^{XY} to denote the cross-spectrum of *X* and *Y*, but we will often refer to this quantity in the text with the shorthand *XY*.

unlikely to be a statistical fluctuation of an underlying parity-even distribution if the assumptions of the DUSTFILAMENTS code represent the true sky.

1.3. Cosmic Birefringence

Cosmic birefringence is an observable consequence of certain types of parity-violating physics beyond the Standard Model and manifests as a rotation of the plane of linear polarization of photons (Carroll et al. 1990; Harari & Sikivie 1992; Carroll 1998). A popular source of cosmic birefringence is an electromagnetically coupled axion-like field, which can behave as both dark matter and dark energy (Marsh 2016). In the CMB, the polarization rotation can be detected as an *EB* correlation (Lue et al. 1999; Feng et al. 2005, 2006; Liu et al. 2006). A *TB* correlation should also be produced, but it is typically a less sensitive observable on account of the large cosmic variance in *T*.

There are several species of cosmic birefringence that have been investigated in the literature. An isotropic, static cosmic birefringence manifests as an overall polarization rotation by the same angle along every line of sight. This observable is, unfortunately, degenerate with a miscalibration of the instrumental polarization orientation (Yadav et al. 2010). The degeneracy is sometimes exploited as a means of "self-calibration" by assuming a standard cosmology in which the true *EB* vanishes (Keating et al. 2013). Although this type of calibration removes sensitivity to an isotropic, static cosmic birefringence, it is still possible to search for cosmic birefringence that is anisotropic (Ade et al. 2015; BICEP2 Collaboration et al. 2017; Bianchini et al. 2020; Namikawa et al. 2020) or time-variable (BICEP/Keck et al. 2021, 2022; Ferguson et al. 2022). Through a campaign of modeling and calibration, it is possible to account for instrumental systematics and measure the isotropic, static cosmic-birefringence angle. Recent measurements of this kind are consistent with a standard cosmology (Kaufman et al. 2014; Planck Collaboration et al. 2016d; Gruppuso et al. 2016; Choi et al. 2020).

A new technique was proposed in Minami et al. (2019), who exploited the fact that the Galactic foregrounds are subject only to polarization miscalibration and not to cosmic birefringence. The observed CMB is rotated by both miscalibration and a possible cosmic birefringence. With measurements at multiple frequencies, the calibration angles and the cosmic-birefringence angle can be extracted simultaneously. Applied to Planck 2018 polarization data (Planck Collaboration et al. 2020b), a cosmic-birefringence angle $\beta = 0.^\circ35 \pm 0.^\circ14$, a discrepancy with the null hypothesis with a significance of 2.4σ, was reported in Minami & Komatsu (2020) under the assumption of a vanishing dust *EB*. With the newer Planck maps produced by the NPIPE pipeline (Planck Collaboration et al. 2020c), the same prescription produced $\beta = 0.^\circ30 \pm 0.^\circ11$, as reported in Diego-Palazuelos et al. (2022). Recently, a similar analysis that includes WMAP polarization data (Bennett et al. 2013) produced the consistent but stronger result $\beta = 0.^\circ342^{+0.^\circ094}_{-0.^\circ091}$ (Eskilt & Komatsu 2022). In these two recent cosmic-birefringence analyses, the impact of a possible foreground *EB* correlation was incorporated by two different approaches, one of which was based on the filamentary misalignment paradigm of Huffenberger et al. (2020) and Clark et al. (2021). When accounting for a possible foreground *EB*, the birefringence angle varies as a function of sky fraction but remains positive. Diego-Palazuelos et al. (2022) refrained from an estimate of statistical significance due to the currently limited understanding of foreground polarization, while Eskilt & Komatsu (2022) quoted a significance of 3.6σ but acknowledged that the foreground polarization must be better understood to be confident that the measured *EB* is cosmological rather than Galactic. The study of magnetic misalignment is, therefore, of central importance in the search for cosmic birefringence.

1.4. Outline

In Section 2, we describe the data products used throughout the analysis. In Section 3, we introduce a new filamentary polarization template that relies on the Hessian matrix of H I intensity maps. In Section 4, we present our misalignment ansatz, i.e., our assumptions of how misalignment perturbs the dust polarization in both map space and harmonic space. We derive misalignment estimators in terms of the auto- and cross-spectra of the Planck dust maps and the H I-based polarization templates, and we test some immediate consequences of these relations. In Section 5, we describe a set of mock skies that we have used to check our estimators. These mock skies are constructed to match the two-point statistics of the Planck dust maps, including cross-spectra with the H I template. In Section 6, we introduce a map-based misalignment estimator and present tentative evidence for a global misalignment angle of $\sim2^\circ$. In Section 7, we divide the sky into small patches and present evidence for scale independence (harmonic coherence) of magnetic misalignment, as well as evidence of spatial coherence. In Section 8, we present evidence for a scale-independent relation between magnetic misalignment and parity-violating cross-spectra such as *TB* and *EB*. We close in Section 9 with suggestions for improvements in our analysis and new directions to further the investigation of parity violation in Galactic dust polarization.

2. Data

We use the Planck Commander dust maps (Planck Collaboration et al. 2020d) as our fiducial measurements of the on-sky thermal dust emission in Stokes *T*, *Q*, and *U*. The maps are constructed by component separation applied to the nine Planck frequency maps, whose passband centers span 30–857 GHz, though polarization is available only for the seven bands spanning 30–353 GHz. Half-mission maps are available and constructed using data exclusively from either the first or second half of the Planck observation period. When forming cross-spectra, we will often use these half-mission splits in order to avoid positive-definite noise biases.

In this work, our H I template is derived from the HI4PI survey (HI4PI Collaboration et al. 2016), a set of full-sky maps of the 21 cm hyperfine transition with an angular resolution of $16.'2$, a sensitivity $\sigma_{\rm rms} = 43$ mK, and a velocity (spectral) resolution of $\delta v = 1.49$ km s^{-1}. The HI4PI survey is a combination of the Parkes Galactic All-Sky Survey (GASS; McClure-Griffiths et al. 2009) and the Effelsberg-Bonn H I Survey (EBHIS; Winkel et al. 2016). The GASS observations cover the southern sky in the velocity range -470 km s^{-1} $\leqslant v_{\rm lsr}$ $\leqslant 470$ km s^{-1}, and the EBHIS observations cover the northern sky in the velocity range -600 km s^{-1} $\leqslant v_{\rm lsr} \leqslant 600$ km s^{-1}. At high Galactic latitudes, nearby dust is generally expected to be associated with lower-velocity H I emission, i.e., with small $|v_{\rm lsr}|$, so our dust-polarization template is drawn from the range -15 km s^{-1} $\leqslant v_{\rm lsr} \leqslant 4$ km s^{-1}, a choice that is motivated in more detail in Section 3.1.

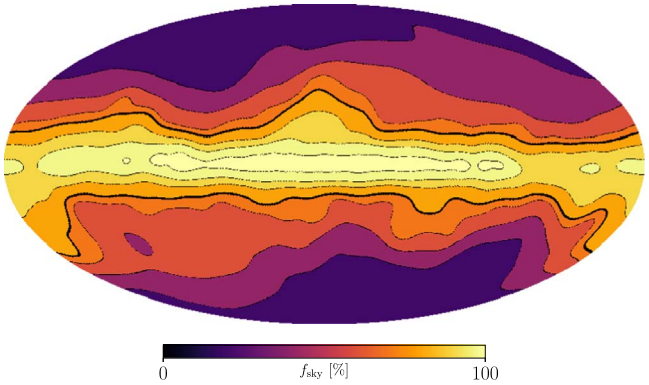

Figure 1. Galaxy masks described in Section 2.1. Each color indicates the sky fraction $f_{\rm sky}$, where the darker colors are meant to be subsumed by the masks associated with the lighter colors. The 70% mask, which is our fiducial choice in much of the analysis, is indicated by the thicker black boundaries.

We compute purified power spectra with `NaMaster` (Alonso et al. 2019) using a C^2 apodization window (Grain et al. 2009) with a scale of 1°. Before computing the power spectra, we smooth the `Commander` maps to 16′.2, the HI4PI beamwidth. We use a `HEALPix` pixelization scheme (Górski et al. 2005) and downgrade all maps to $N_{\rm side} = 256$ for faster power-spectrum estimation. We spot-check some of our results at higher $N_{\rm side}$ and find that they are consistent.

2.1. Galaxy Masks

We use the Galaxy masks provided by the Planck Legacy Archive.[5] These masks are constructed to limit Galactic emission to varying levels. The masks with a smaller sky fraction $f_{\rm sky}$ restrict the analysis to relatively high latitudes. The masks with larger $f_{\rm sky}$ allow more contributions from nearer to the Galactic plane. The set of Galaxy masks is shown in Figure 1. Our fiducial mask in much of the analysis is defined by $f_{\rm sky} = 70\%$, and we will refer to it as the "70% Galaxy mask."

2.2. Notation

We use the subscript "H I" to denote quantities derived from the H I-based polarization template. For example, the H I-based prediction for dust E modes is denoted by $E_{\rm H\,I}$. It is important to note that these quantities are describing H I-based predictions for the polarization of dust rather than the polarization properties of the H I itself. The H I is measured in total (unpolarized) intensity, and prescriptions like the Hessian method of Section 3 convert those intensity maps into dust polarization templates.

We use the subscript "d" to denote quantities related to Galactic dust. Usually, this will refer specifically to the Planck `Commander` maps described above.

2.3. Bandpass Filtering

Much of our analysis is restricted to $\ell > 100$, and we often form maps that are bandpass-filtered. We filter by applying an ℓ-dependent Tukey window to the spherical-harmonic representation of the maps. We use a taper of length $t_\ell = 50$, which produces a flat-topped passband when the window width is larger than $2t_\ell$. We test these filters on full-sky Planck dust maps and find the out-of-band response to be suppressed by a factor of more than 10^4. In particular, the out-of-band leakage is below the level of the high-latitude dust power (computed on the Planck 70% Galaxy mask), even when the filtered power spectra are computed on the full sky, i.e., including the Galactic plane.

3. Hessian Method

We introduce a new Hessian-based filament-finding algorithm (similar to those of, e.g., Planck Collaboration et al. 2016b; Kalberla et al. 2021). Whereas previous work on misalignment (Clark et al. 2021) used a filamentary model based on the RHT (Clark et al. 2014; Clark & Hensley 2019), we find that our new Hessian-based polarization template correlates more strongly with Planck measurements of B-mode dust polarization for $\ell \gtrsim 100$ (Figure 17 in Appendix A). Furthermore, whereas the RHT loses its correlation with the Planck B modes for $\ell \gtrsim 400$, the Hessian maintains a correlation of ∼10% up to our highest multipoles ($\ell_{\rm max} = 767$). In the E modes, the two methods correlate with Planck at roughly equivalent levels.

We additionally prefer the Hessian method for its relative computational efficiency. The Hessian method requires only two operations in spherical-harmonic space, while the RHT requires a suite of convolutions to sample polarization angles. Direct comparisons will be presented in future work (G. Halal et al. 2022, in preparation).

The Hessian matrix contains information about the local second derivatives. By searching for regions of negative curvature in an intensity map, we find candidate filaments. Negative curvature implies that at least one of the Hessian eigenvalues is negative. The orientation of the filament is determined by the local eigenbasis. As in, e.g., Clark et al. (2015), we assume that the POS filament is aligned with the POS magnetic field. The dust polarization is taken to be orthogonal to the filament. With these assumptions, we can convert an intensity map into a polarization template.

Hessian-based filament identifications have been performed on, e.g., 353 GHz maps in Planck Collaboration et al. (2016a, 2016b), HI4PI H I and Planck 857 GHz maps in Kalberla et al. (2021), Herschel images of molecular clouds (Polychroni et al. 2013), and simulations of the cosmic web (Colombi et al. 2000; Forero-Romero et al. 2009). In addition to the RHT, some non-Hessian filament-finding algorithms that have been applied to studies of the ISM include `DisPerSE` (Arzoumanian et al. 2011; Sousbie 2011) and `getfilaments` (Men'shchikov 2013). See Section 3.10 of Hacar et al. (2022) for a more comprehensive review.

3.1. Prescription

We use the Hessian matrix to identify filament orientations. To construct H I-based templates for dust polarization, we form weights from the Hessian eigenvalues.

We analyze the H I maps in individual velocity bins. Our final polarization template is produced by summing over velocities. The H I intensity in velocity channel v is denoted I_v. We work in spherical coordinates with polar angle θ and

[5] pla.esac.esa.int

azimuthal angle ϕ. The local Hessian matrix is given by

$$H \equiv \begin{pmatrix} H_{xx} & H_{xy} \\ H_{yx} & H_{yy} \end{pmatrix}, \tag{2}$$

where

$$H_{xx} = \frac{\partial^2 I_v}{\partial \theta^2}, \tag{3}$$

$$H_{yy} = \frac{1}{\sin^2\theta}\frac{\partial^2 I_v}{\partial \phi^2}, \tag{4}$$

$$H_{xy} = H_{yx} = -\frac{1}{\sin\theta}\frac{\partial^2 I_v}{\partial \phi \partial \theta}. \tag{5}$$

The eigenvalues are

$$\lambda_{\pm} = \frac{1}{2}(H_{xx} + H_{yy} \pm \alpha), \tag{6}$$

where

$$\alpha \equiv \sqrt{(H_{xx} - H_{yy})^2 + 4H_{xy}^2}. \tag{7}$$

The candidate polarization angle is then

$$\theta_v = \arctan\left(\frac{H_{xx} - H_{yy} + \alpha}{2H_{xy}}\right), \tag{8}$$

but we will enforce conditions below to ensure this identification is sensible.

First, for the local curvature to be negative along at least one axis, we need $\lambda_- < 0$. Second, we want this negative curvature to be the dominant local morphology, so we require λ_- to be the larger of the two eigenvalues in magnitude. Define

$$\Delta\lambda \equiv |\lambda_-| - |\lambda_+|. \tag{9}$$

Then we define the velocity-dependent weight

$$w_v \equiv |\lambda_-|[\Delta\lambda > 0][\lambda_- < 0], \tag{10}$$

where the Iverson brackets on the right-hand side enforce conditions on $\Delta\lambda$ and λ_-.[6]

Our velocity-dependent Stokes templates are given by

$$T_v(\hat{\boldsymbol{n}}) \equiv w_v(\hat{\boldsymbol{n}}), \tag{11}$$

$$Q_v(\hat{\boldsymbol{n}}) \equiv w_v(\hat{\boldsymbol{n}})\cos[2\theta_v(\hat{\boldsymbol{n}})], \tag{12}$$

$$U_v(\hat{\boldsymbol{n}}) \equiv w_v(\hat{\boldsymbol{n}})\sin[2\theta_v(\hat{\boldsymbol{n}})]. \tag{13}$$

The Hessian method is susceptible to small-scale noise and scan artifacts, so we restrict our analysis to the HI4PI velocity bins with greatest sensitivity. We start with the binning of Clark & Hensley (2019). As a proxy for noisiness, we search for pixels with intensities that are reported to be negative. We remove any velocity slice that contains negative-intensity pixels on the Planck 70% Galaxy mask. This leaves a continuous range between -15 and 4 km s^{-1}. The velocity selection is intended to avoid numerical pathologies and should be revisited in a future iteration of the Hessian algorithm. Most of the H I emission is at low velocities (see, e.g., Figure 1 of Clark & Hensley 2019), so we are retaining the dominant contributions even with the current velocity cuts. The velocity cut affects our analysis mainly in terms of sensitivity, since there is potentially useful information about dust filaments in the velocity slices that are discarded. In general, sensitivity is greater when the H I template correlates more strongly with Planck dust polarization. We defer to future work an investigation of the potential improvements from differently chosen velocity cuts (G. Halal et al. 2022, in preparation). We repeated a majority of the following calculations with the RHT-based template (Appendix A) that uses the much broader velocity range of -90 to 90 km s^{-1} as in Clark & Hensley (2019), and we find consistent results. The full templates are given by

$$X_{\mathrm{H\,I}}(\hat{\boldsymbol{n}}) \equiv \sum_v X_v(\hat{\boldsymbol{n}}) \tag{14}$$

for $X \in \{T, Q, U\}$.

An illustration of our Hessian method is provided in Figure 2, where we analyze a region with area $10^\circ \times 10^\circ$ centered on $(l, b) = (12^\circ, 45^\circ)$. The velocity bin is centered on -4.4 km s^{-1} with a width of 1.3 km s^{-1}. The panels of Figure 2 show how the raw HI4PI intensity map is transformed into a filamentary intensity w_v and how the filament orientations determine the inferred magnetic-field orientations.

Additional material related to our Hessian method is provided in Appendix A.

4. Misalignment Ansatz

As an ansatz for the observable signature of magnetic misalignment, we assume a multipole-dependent rotation angle ψ_ℓ as in Clark et al. (2021). We denote the observed E and B modes by $E(\ell)$ and $B(\ell)$ and the unphysical modes that would be observed in the absence of misalignment by $\tilde{E}(\ell)$ and $\tilde{B}(\ell)$, where ℓ identifies a particular spherical harmonic with multipole moment ℓ. Our ansatz takes the form

$$\begin{pmatrix} E(\ell) \\ B(\ell) \end{pmatrix} = \begin{pmatrix} \cos(2\psi_\ell) & -\sin(2\psi_\ell) \\ \sin(2\psi_\ell) & \cos(2\psi_\ell) \end{pmatrix} \begin{pmatrix} \tilde{E}(\ell) \\ \tilde{B}(\ell) \end{pmatrix}. \tag{15}$$

For the purposes of the ansatz, we are imagining that all of the dust polarization participates in the misalignment. As mentioned in Section 1.2, this assumption is likely inaccurate, since some of the dust morphology is nonfilamentary. Later, we will form estimators by comparing the observed dust polarization with the predictions of the H I template, and this will restrict the analysis to the filamentary modes that we do expect to be described by the ansatz of Equation (15) (in the misalignment paradigm).

To make magnetic misalignment less abstract, we provide an illustration in Figure 3. We consider perfect alignment (black) and scale-independent misalignment (green). Perfect alignment is assumed by the H I-based filamentary model of dust polarization (Section 1.2). For scale-independent misalignment, we take $\psi_\ell = 20^\circ$ for all ℓ. This is a much larger misalignment than we expect to measure on the true sky, but the exaggeration is useful for visualization. In this case, the magnetic field shows a consistent rotation by the same amount and with the same sense relative to the H I template.

[6] For a statement p, the Iverson bracket $[p]$ is 1 when p is true and zero when p is false (Iverson 1962; Knuth 1992).

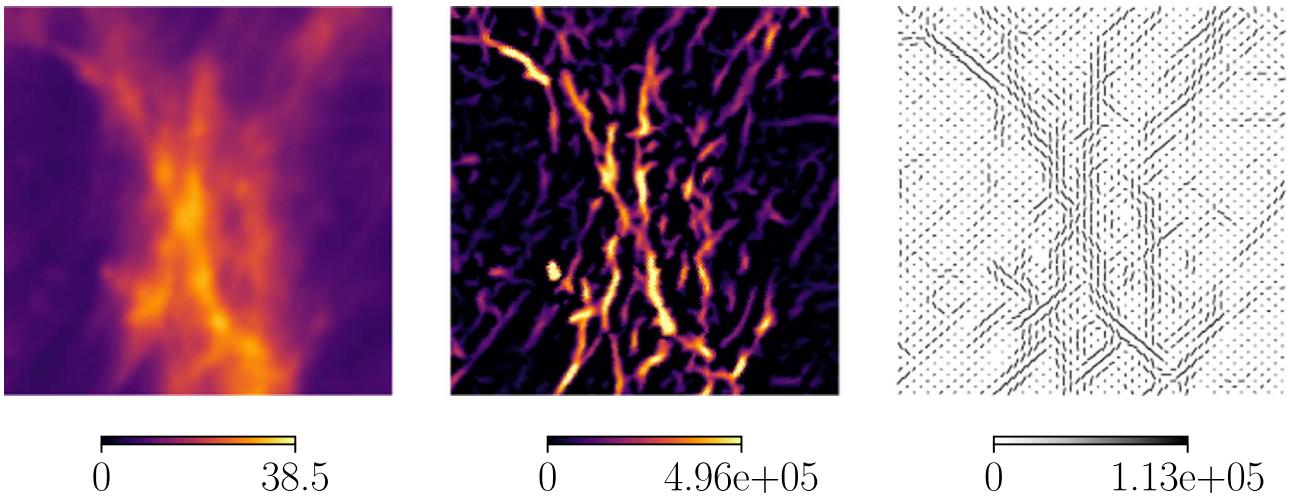

Figure 2. Illustration of the Hessian-based filament-finding algorithm (Section 3) on a sky region of area $10^\circ \times 10^\circ$ centered on $(l, b) = (12^\circ, 45^\circ)$ in a velocity bin centered on -4.4 km s^{-1} with a width of 1.3 km s^{-1}. The units for all panels are K km s^{-1}, but note that the right two panels are produced by taking second derivatives of intensity with respect to angular coordinates in radians. (Left) Raw HI4PI intensity. (Middle) Hessian intensity T_v (Equation (11)), which upweights regions of negative curvature and produces structure that is visually filamentary. (Right) Hessian-derived magnetic-field orientations (orthogonal to the polarization angle θ_v from Equation (8)) tracing the orientation of the filaments.

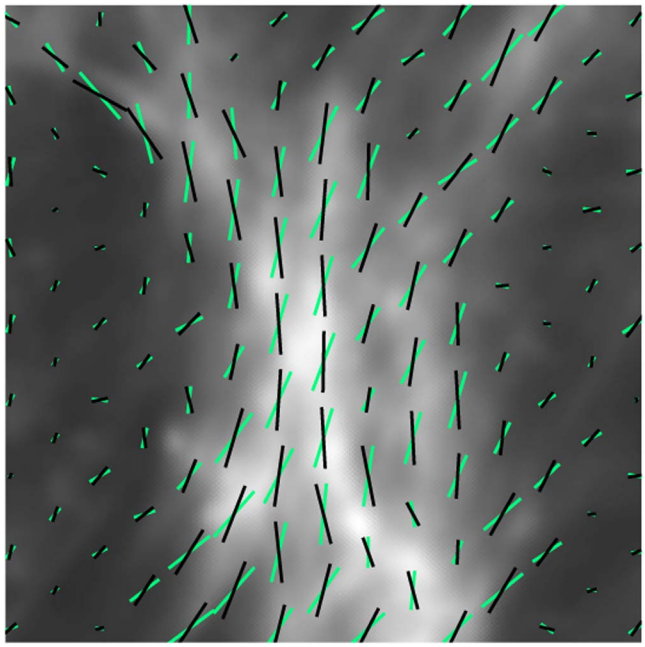

Figure 3. Illustration of magnetic misalignment. (Black) Magnetic-field orientations derived from our H I template for the same sky region and velocity bin as in Figure 2 but downgraded to $N_{\rm side} = 64$. The pseudovector lengths are proportional to the template-implied polarization intensity. (Green) The same after applying a global misalignment angle $\psi = 20^\circ$, which is an unrealistically large amplitude for better visualization. (Gray-scale color map) Raw H I intensity map (identical to the left panel of Figure 2).

4.1. Assumptions

The H I-based filamentary model of dust polarization assumes perfect alignment. We observe in Appendix A.3 that the H I model displays no intrinsic parity violation. We therefore assume that $E_{\rm H\,I}$ correlates with $\tilde{E}_{\rm d}$ but not with $\tilde{B}_{\rm d}$, and we make a symmetric assumption for $B_{\rm H\,I}$. Our assumptions are summarized by

$$D_\ell^{E_{\rm H\,I}\tilde{B}_{\rm d}} = D_\ell^{B_{\rm H\,I}\tilde{E}_{\rm d}} = D_\ell^{T_x\tilde{B}_{\rm d}} = 0 \tag{16}$$

for $x \in \{\rm H\,I, d\}$.

4.2. Implications for Cross-spectra

With Equations (15) and (16), we can derive the following relations between observable cross-spectra in terms of the misalignment angle ψ_ℓ:

$$D_\ell^{E_{\rm H\,I}B_{\rm d}} = \tan(2\psi_\ell) D_\ell^{E_{\rm H\,I}E_{\rm d}}, \tag{17}$$

$$D_\ell^{B_{\rm H\,I}E_{\rm d}} = -\tan(2\psi_\ell) D_\ell^{B_{\rm H\,I}B_{\rm d}}, \tag{18}$$

$$D_\ell^{T_xB_{\rm d}} = \tan(2\psi_\ell) D_\ell^{T_xE_{\rm d}}, \tag{19}$$

and

$$D_\ell^{E_{\rm d}B_{\rm d}} = \frac{1}{2}\tan(4\psi_\ell)(D_\ell^{E_{\rm d}E_{\rm d}} - D_\ell^{B_{\rm d}B_{\rm d}}). \tag{20}$$

From the known positive $T_{\rm d}B_{\rm d}$ and $T_{\rm d}E_{\rm d}$ measured by Planck (Section 1.1), we expect ψ_ℓ to be mostly positive in the range $100 \lesssim \ell \lesssim 500$ on large sky areas away from the Galactic plane, e.g., with a 70% Galaxy mask (Clark et al. 2021). We also know that $E_{\rm H\,I}E_{\rm d} > 0$, $B_{\rm H\,I}B_{\rm d} > 0$ (Clark & Hensley 2019), and $E_{\rm d}E_{\rm d} > B_{\rm d}B_{\rm d}$ (Planck Collaboration et al. 2016c) across the same multipole range and on the same sky area. Our qualitative expectations, then, are to find $E_{\rm H\,I}B_{\rm d}$, $T_{\rm H\,I}B_{\rm d}$, and $E_{\rm d}B_{\rm d}$ to be positive but $B_{\rm H\,I}E_{\rm d}$ to be negative.

We can make simple estimates of ψ_ℓ with Equations (17)–(19), though each is potentially biased by noise in the denominator:

$$\tan(2\psi_\ell) = \frac{D_\ell^{E_{\rm H\,I}B_{\rm d}}}{D_\ell^{E_{\rm H\,I}E_{\rm d}}} = -\frac{D_\ell^{B_{\rm H\,I}E_{\rm d}}}{D_\ell^{B_{\rm H\,I}B_{\rm d}}} = \frac{D_\ell^{T_{\rm H\,I}B_{\rm d}}}{D_\ell^{T_{\rm H\,I}E_{\rm d}}} = \frac{D_\ell^{T_{\rm d}B_{\rm d}}}{D_\ell^{T_{\rm d}E_{\rm d}}}. \tag{21}$$

We could form a similar estimate from Equation (20), but the $E_{\rm d}B_{\rm d}$ measurement from Planck is especially noisy, so we ignore it for the remainder of this section. The four cross-spectrum ratios in Equation (21) allow for tests of the misalignment ansatz without explicit calculation of ψ_ℓ.

While positive $T_{\rm H\,I}B_{\rm d}$ and $E_{\rm H\,I}B_{\rm d}$ might be anticipated on account of the known positive $T_{\rm d}B_{\rm d}$, $T_{\rm d}T_{\rm H\,I}$, $T_{\rm d}E_{\rm d}$, and $E_{\rm H\,I}E_{\rm d}$, it

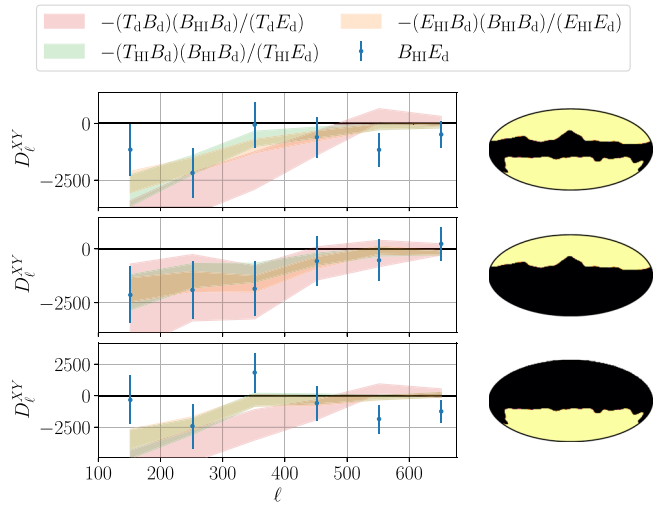

Figure 4. The $B_{\rm H\,I}E_{\rm d}$ cross-spectrum measured on the Planck 70% Galaxy mask. The spectra are shown for the full mask (top), the northern hemisphere of that mask (middle), and the southern hemisphere (bottom). The shaded bands show three different expectations for $B_{\rm H\,I}E_{\rm d}$ based on other measured spectra (Equation (21)). The units are $\mu{\rm K_{RJ}}$ K km s^{-1}, and the error bars and bands are derived from Gaussian variances. The expectations and measurements show a broad consistency, in particular, the tendency for $B_{\rm H\,I}E_{\rm d} < 0$, which persists in each hemisphere independently.

is, in principle, possible for the $T_{\rm d}B_{\rm d}$ signal to be entirely decoupled from the H I-correlated components of the dust maps. In Section 5, we describe how to construct mock skies with exactly this property. These mock skies show positive $T_{\rm d}B_{\rm d}$ but zero $T_{\rm H\,I}B_{\rm d}$ and zero $E_{\rm H\,I}B_{\rm d}$. While we consider $T_{\rm H\,I}B_{\rm d}$, $E_{\rm HI}B_{\rm d} > 0$ to be the most plausible expectation, it is formally nontrivial.

The negativity of $B_{\rm H\,I}E_{\rm d}$ is a new prediction of the misalignment ansatz. We can make quantitative predictions for this signal (Equation (21)), and comparisons are shown in Figure 4 for our fiducial 70% Galaxy mask (Section 2.1). We mentioned above that we expect ψ_ℓ to be smooth over the multipole range $100 \lesssim \ell \lesssim 500$, so we expect $B_{\rm H\,I}E_{\rm d}$ to be smooth over similar multipoles. We can, therefore, gain in per-bandpower sensitivity by using the relatively large bin width of $\Delta\ell = 100$.

In Figure 4, we find that $B_{\rm H\,I}E_{\rm d}$ tends negative and is broadly consistent with the expectations of Equation (21) over the full mask and in the northern and southern hemispheres independently. Due to the unavailability of suitable dust and H I simulations, we do not attempt a statistical evaluation of the consistency. The plotted error bars are derived from Gaussian variances. As the dust field displays both non-Gaussianity and statistical anisotropy, these variances are meant only as a rough indication of the fidelity of the measurements.

We expect $B_{\rm H\,I}E_{\rm d}$ to be noisier than $E_{\rm H\,I}B_{\rm d}$ and $T_{\rm H\,I}B_{\rm d}$ because $r_\ell^{B_{\rm H\,I}B_{\rm d}}$ is smaller (by roughly a factor of 2–3 for $\ell > 100$) than $r_\ell^{E_{\rm H\,I}E_{\rm d}}$ and $r_\ell^{T_{\rm H\,I}T_{\rm d}}$; i.e., $B_{\rm H\,I}$ is a less accurate representation of $B_{\rm d}$ than $E_{\rm H\,I}$ or $T_{\rm H\,I}$ is of $E_{\rm d}$ or $T_{\rm d}$, respectively. The H I-based polarization template is, therefore, more sensitive to $\tilde{E}_{\rm d}$ modes mixed into the observed $B_{\rm d}$ than to $\tilde{B}_{\rm d}$ modes mixed into $E_{\rm d}$ (Equation (15)).

We consider the results of Figure 4 to be a first step in confirming that the misalignment ansatz of Equation (15) is at least a partial description of the true sky. These results avoided an explicit calculation of the misalignment angle ψ_ℓ. In later sections, we will compute ψ_ℓ directly.

5. Mock Skies

We construct a set of mock-sky realizations in order to check for biases and spurious signals in the estimators that we will introduce in subsequent sections. We maintain the two-point statistics of the true sky including correlations with the H I-based polarization templates. These mock skies are phenomenological in the sense that they produce realistic observables without explicit appeal to the underlying ISM physics; in particular, these are not numerical ISM simulations.

Our mock skies include Gaussian noise, an H I-based filamentary component, and Gaussian dust. We arrange for all of the two-point statistics to be the same as for the true sky; i.e., the mock skies replicate the measured X_aY_b for $X, Y \in \{T, E, B\}$ and $a, b \in \{{\rm d}, {\rm H\,I}\}$. The H I-based component is the same for all realizations and derived from the true-sky Hessian template (Section 3).

In harmonic space, we express the mock-sky (S) map as a linear combination of an ℓ-filtered H I template, a Gaussian dust component (G), and a Gaussian noise component (N),

$$X_S(\ell) = k_\ell^{(X)} X_{\rm H\,I}(\ell) + X_G(\ell) + X_N(\ell), \tag{22}$$

for $X \in \{T, E, B\}$, where $X_{\rm H\,I}(\ell)$ is the harmonic-space representation of the Hessian template (Section 3). The ℓ-dependent coefficient in the H I term is necessary because $D_\ell^{X_{\rm H\,I}X_{\rm H\,I}} \propto D_\ell^{X_{\rm H\,I}X_{\rm d}}$. To maintain $D_\ell^{X_{\rm H\,I}X_S} = D_\ell^{X_{\rm H\,I}X_{\rm d}}$, we modify with the transfer function $k_\ell^{(X)}$ (Appendix A.2), which ensures consistency with the true H I–Planck cross-spectra. While the H I term is constant across realizations and based on the true sky, the Gaussian dust and noise are stochastic.

The power spectra of the Gaussian dust and noise components are estimated from the measured dust and H I power spectra. We calculate these spectra after applying the 70% Galaxy mask. We compute $X_{\rm H\,I}(\ell)$ from a masked map as well. As a result, the mock skies are well defined only on the unmasked 70% of the celestial sphere.

Unlike the CMB, Galactic dust emission is statistically anisotropic; i.e., the statistics of the dust are different in different regions of the sky. We approximate the nonstationarity by beginning with Gaussian noise and dust that are isotropic and then modulating based on the statistical anisotropies in the `Commander` maps. The modulation is performed on scales much larger than those used in our analysis. The modulation field is smoothed to $14\overset{\circ}{.}7$, twice the side length of a pixel with $N_{\rm side} = 8$, while most of our analysis is concerned with multipoles $\ell > 100$, i.e., degree scales and smaller. We therefore expect negligible mode mixing.

A realization of the modulated dust mock sky is shown in Figure 5 after high pass filtering to $\ell > 100$, the multipole range targeted by most of our analysis. Before filtering, the mock skies are dominated by large-scale modes, which are bright and relatively poorly estimated, but those large-scale modes are irrelevant for most of our analysis. Visually, we find greater non-Gaussianity in the real $T_{\rm d}$ map than in the mock sky. The polarization maps bear a greater resemblance to each other. A higher level of realism is unnecessary, since we use these mock skies only to check for biases in our estimators.

A breakdown of the mock-sky components is shown in Figure 6, where we see that most of the dust power is in the Gaussian rather than the H I component.

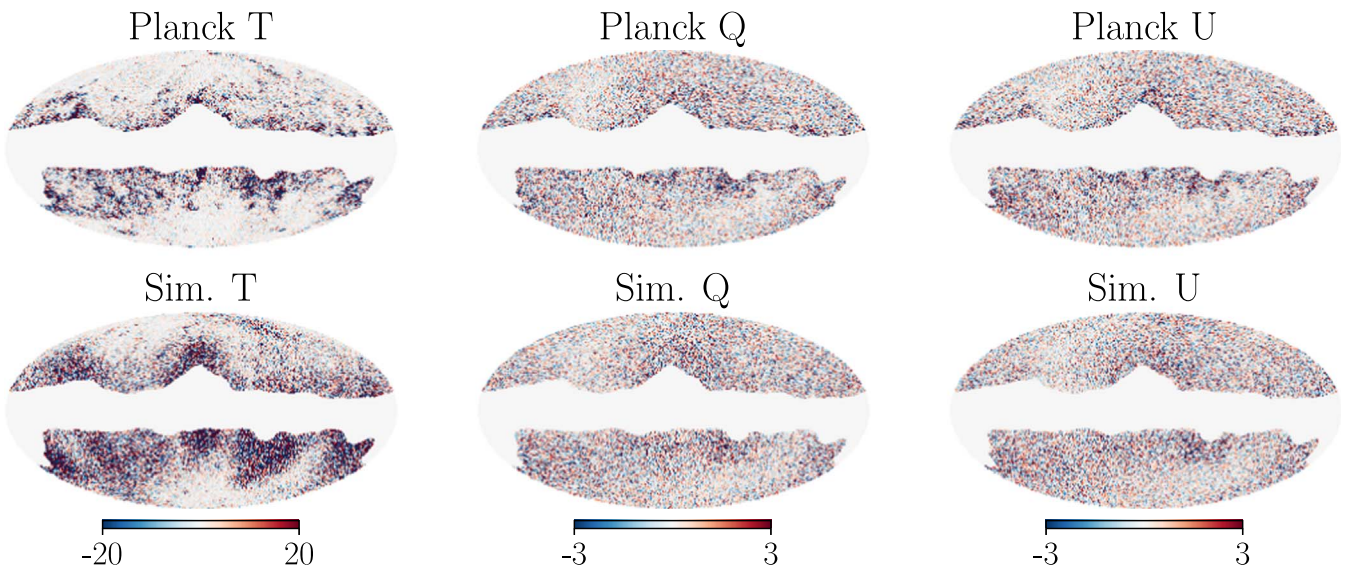

Figure 5. Realization of the modulated Gaussian mock skies (Section 5) after high pass filtering to $\ell > 100$. The units of the color scales are μK_{RJ}. The modulated Gaussianity adds an additional level of realism to the mock skies, but the strongly non-Gaussian features, especially in the Planck T_d map, are not captured. These mock skies are used only for basic estimator tests, not for statistical inference.

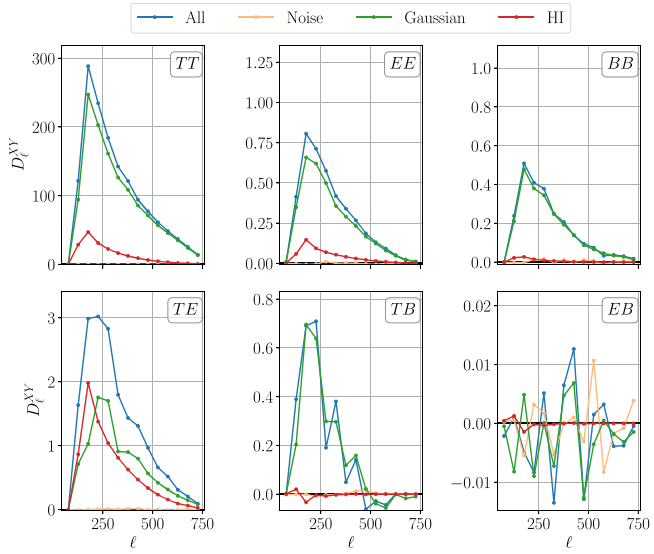

Figure 6. Breakdown of mock-sky components in power-spectrum space for the modulated-Gaussian realization shown in Figure 5 (with the same high pass filtering to $\ell > 100$). The vertical axis units are μK_{RJ}^2. The annotations indicate the spectrum type, e.g., *TT* for the upper left plot. Blue shows the half-mission cross-spectrum $\tilde{D}_\ell^{XY}$ (Equation (23)). Orange shows the half-mission noise cross-spectrum. The Gaussian dust spectrum is shown in green, and the H I spectrum is shown in red. We note that the H I-correlated component represents a minority contribution to all of the spectra except *TE*, which is a characteristic signature of a filamentary magnetically aligned polarization model.

We note that the unbiased power-spectrum estimator

$$\tilde{D}_\ell^{XY} \equiv \frac{1}{2}(D_\ell^{X^{(1)}Y^{(2)}} + D_\ell^{X^{(2)}Y^{(1)}}) \tag{23}$$

is crucial for avoiding a large noise bias in polarization, especially for $\ell \gtrsim 200$. The H I component shows negligible *TB* and *EB* but strong *TE*, which is arguably a defining characteristic of the filamentary polarization model. Although the Gaussian component dominates in *TT*, *EE*, and *BB*, the H I component accounts for roughly half of the *TE* signal.

We verified that the two-point statistics of the mock skies are approximately equivalent to those of the true dust maps. In particular, we check that $X_S Y_S$ (where S denotes a mock sky) matches $X_d Y_d$ and that $X_{HI} Y_S$ matches $X_{HI} Y_d$. The agreement is sufficient to test the estimators that we will introduce below.

We emphasize that our mock-sky framework is not intended to represent a null hypothesis for the purposes of statistical inference. In particular, the mock skies are missing much of the non-Gaussian structure in the true sky, even beyond the H I-correlated component. Instead, because no aggregate misalignment has been input, these mock skies are useful for testing our estimators for spurious signals.

6. Misalignment Estimator

We present an estimator for the misalignment angle of a region of sky containing multiple pixels. In Clark et al. (2021), the angle difference between the dust and the H I template was computed by

$$\Delta\theta \equiv \frac{1}{2}\text{atan2}[c_{HI} s_d - s_{HI} c_d,\, c_{HI} c_d + s_{HI} s_d], \tag{24}$$

where $c_x \equiv \cos(2\theta_x)$ and $s_x \equiv \sin(2\theta_x)$.[7] While Equation (24) measures the misalignment angle of a single pixel, care must be taken in computing the mean over multiple pixels because $\Delta\theta$ is a circular statistic. The values of $\Delta\theta$ are restricted to $[-90°, 90°]$, but the end points of this range are physically identical. Naively averaging random values from this range will produce mean values that cluster near zero instead of being uniformly distributed. As a result, noise fluctuations produce a multiplicative bias that suppresses the magnitude of $\langle\Delta\theta\rangle$.

To account for the circularity of $\Delta\theta$, we use a modified version of the projected Rayleigh statistic (Jow et al. 2017), which is itself a form of alignment estimator (see Section 6.2 of Clark & Hensley 2019). The essence of the method is to consider terms of the form $\cos[2(\theta_d(\hat{\boldsymbol{n}}) - \theta_{HI}(\hat{\boldsymbol{n}})) - \psi]$, where

[7] We use the two-argument arctangent (satan2) to avoid quadrant ambiguities in the angle determination.

$\theta_{\rm d}(\hat{\boldsymbol{n}})$ is the polarization angle measured by Planck, $\theta_{\rm H\,I}(\hat{\boldsymbol{n}})$ is the angle predicted by the H I template, and ψ is a free parameter independent of $\hat{\boldsymbol{n}}$ and representing the misalignment angle. We sum such terms over the selected map pixels $\hat{\boldsymbol{n}}$ and maximize with respect to ψ. Denote the maximizing value by $\hat{\psi}$. When $\theta_{\rm d}(\hat{\boldsymbol{n}}) - \theta_{\rm H\,I}(\hat{\boldsymbol{n}})$ is random, $\hat{\psi}$ is also random. This is a plausibility argument that $\hat{\psi}$ is unbiased, but we will describe an explicit test below.

Rather than simply summing the cosine terms described above, we upweight pixels with a higher signal-to-noise ratio in polarization. The weights are proportional to the product of the signal-to-noise ratios for Planck and HI4PI. Denote the per-pixel weight by $w(\hat{\boldsymbol{n}})$.

We form the alignment metric

$$\xi(\psi) \equiv \frac{1}{W}\sum_{\hat{\boldsymbol{n}}} w(\hat{\boldsymbol{n}})\cos[2(\theta_{\rm d}(\hat{\boldsymbol{n}}) - \theta_{\rm H\,I}(\hat{\boldsymbol{n}}) - \psi)], \tag{25}$$

where ψ is a free parameter, and $W = \sum_{\hat{\boldsymbol{n}}} w(\hat{\boldsymbol{n}})$. The nonuniform weighting of the contributing pixels distinguishes our alignment metric from that of Section 6.2 of Clark & Hensley (2019), but it is an estimator for the same quantity. We maximize $\xi(\psi)$ with respect to ψ and denote the maximizing value by $\hat{\psi}$.

We can calculate $\hat{\psi}$ analytically with the following prescription. Form

$$A \equiv \frac{1}{W}\sum_{\hat{\boldsymbol{n}}} w(\hat{\boldsymbol{n}})(c_{\rm H\,I}c_{\rm d} + s_{\rm HI}s_{\rm d}), \tag{26}$$

$$B \equiv \frac{1}{W}\sum_{\hat{\boldsymbol{n}}} w(\hat{\boldsymbol{n}})(c_{\rm H\,I}s_{\rm d} - s_{\rm H\,I}c_{\rm d}), \tag{27}$$

where $c_x \equiv Q_x/P_x$ and $s_x \equiv U_x/P_x$. Then we can express the alignment metric as

$$\xi(\psi) = A\cos(2\psi) + B\sin(2\psi), \tag{28}$$

from which the maximizing value can be found to be

$$\hat{\psi} = \frac{1}{2}\mathrm{atan2}(B, A), \tag{29}$$

where, because $A(\theta_{\rm d} = \theta_{\rm H\,I}) > 0$ and $B(\theta_{\rm d} = \theta_{\rm H\,I}) = 0$, this choice of arctangent ensures $\hat{\psi} = 0$ in the case of perfect alignment. In the limit of a single pixel $\hat{\boldsymbol{n}}$, the estimator $\hat{\psi}$ is equivalent to Equation (24), the $\Delta\theta$ used in Clark et al. (2021). The added benefit of $\hat{\psi}$ is in aggregating pixels into patches without biasing the estimates low (as described at the beginning of this section).

6.1. Misalignment Maps

We present maps of $\hat{\psi}$ in Figure 7. We compute $\hat{\psi}$ on masks defined by `HEALPix` pixels with various values of $N_{\rm side}$. For the low-pass-filtered ($\ell < 702$) results in the left column of Figure 7, the misalignment angles are partially correlated between patches due to the presence of large-scale polarization modes. Part of the motivation for the bandpass filtering ($101 < \ell < 702$) implemented for the right column of Figure 7 is to remove these correlations and acquire approximately independent estimates in each patch. For $N_{\rm side} = 32$, the smallest patch size we consider, the side length of each mask is $1\overset{\circ}{.}8$, which means that the above-mentioned bandpass filtering suppresses modes with wavelengths larger than a single patch. Most of the patch-to-patch correlations are removed by the bandpass filtering. (We will show in Section 7.2, however, that there is evidence for nontrivial spatial coherence of $\hat{\psi}$ that cannot be simply attributed to large-scale modes.)

As the patch size decreases, regions of higher and lower variance emerge at all latitudes in a pattern that is similar to that of $\Delta\theta$ in Figure 3 of Clark et al. (2021). The above observations are broadly consistent between the low-pass-filtered ($\ell < 702$) and bandpass-filtered ($101 < \ell < 702$) maps, but the former are visually smoother.

6.2. Test for Estimator Bias

To check for biases in our misalignment estimator, we measure $\hat{\psi}$ on masks defined by `HEALPix` pixels as described above, artificially rotate the angles of the Planck polarization map by a known amount $\psi_0 \in [-90°, 90°]$, and then recompute $\hat{\psi}$. We track the median of the distribution and find that it follows ψ_0. We conclude that $\hat{\psi}$ is an unbiased estimator of misalignment angle.

6.3. Positive Misalignment Tendency

We observe a tendency toward positive misalignment angles in Figure 7. To estimate the statistical significance, it is tempting to appeal to the central limit theorem. Unfortunately, the values of $\hat{\psi}(\hat{\boldsymbol{n}})$, where $\hat{\boldsymbol{n}}$ represents a particular patch, are neither completely independent nor identically distributed. By bandpass filtering to $101 < \ell < 702$ as in the right column of Figure 7, we can achieve approximate independence of the estimates for different $\hat{\boldsymbol{n}}$. We cannot, however, guarantee that the estimates are identically distributed.

Nevertheless, because the calculation is simple, we estimate a mean and standard error by appealing to the central limit theorem. For $N_{\rm side} = 32$, we find $\hat{\psi}_{\ell<702} = 1\overset{\circ}{.}9 \pm 0\overset{\circ}{.}3$, but we caution that the patches are nontrivially correlated with each other by the bright, large-scale polarization modes and, therefore, refrain from claiming any statistical significance. Restricting to the sky area allowed by our fiducial 70% Galaxy mask (see Figure 8), we find $\hat{\psi}_{\ell<702} = 1\overset{\circ}{.}7 \pm 0\overset{\circ}{.}3$. After bandpass filtering, the patches are more (but not completely) independent, and we find $\hat{\psi}_{101<\ell<702} = 0\overset{\circ}{.}9 \pm 0\overset{\circ}{.}3$, which implies a statistical significance of 3σ. Restricting to our fiducial 70% Galaxy mask, we find $\hat{\psi}_{101<\ell<702} = 0\overset{\circ}{.}8 \pm 0\overset{\circ}{.}4$, which implies a significance of 2σ. We have deliberately limited ourselves to a single significant figure because we consider these calculations to be crude estimates.

6.4. Relationship to Dust Properties

We note that the large-scale features of $\hat{\psi}$ are similar to those of the dust polarization fraction $p_{\rm d} \equiv \sqrt{Q_{\rm d}^2 + U_{\rm d}^2}/T_{\rm d}$. For visual comparison, we provide in Figure 9 maps displaying misalignment angle $\hat{\psi}$, dust intensity $T_{\rm d}$, and dust polarization fraction $p_{\rm d}$. We omit an estimate of the correlation strengths because the bright, large-scale modes induce covariances that are difficult to model. The low-column (small-$T_{\rm d}$) sky regions in the northeast and southwest are also regions of increased variance in $\hat{\psi}$, as evidenced by the large fluctuations between neighboring patches, but a much clearer visual correspondence appears between $\hat{\psi}$ and $p_{\rm d}$. The regions of larger $p_{\rm d}$ show smaller variance in $\hat{\psi}$, and those

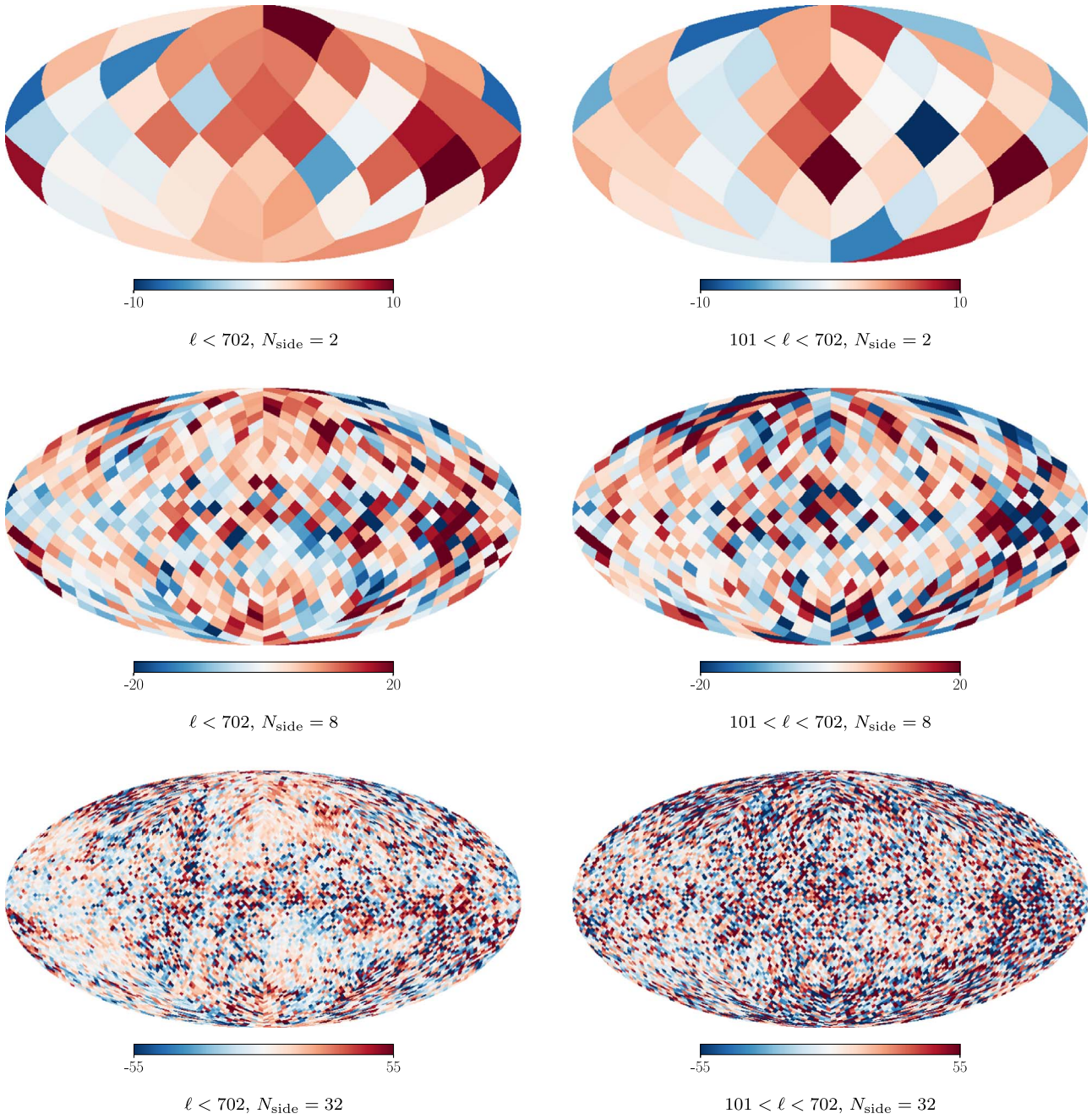

Figure 7. Maps of misalignment angle $\hat{\psi}$ (Equation (29)) on masks defined by pixels with various values for $N_{\rm side}$ and different filtering options. In the left column, the Planck and H I maps have been low-pass-filtered to $\ell < 702$, which is approximately the HI4PI beam scale. In the right column, the maps have been bandpass-filtered to $101 < \ell < 702$, which is the multipole range used for much of the following analysis. The color scales are in degrees. We see greater variance in the northeast (top left) and southwest (bottom right), which are the regions with the lowest dust intensity, and we see a tendency for the misalignment angles to be positive.

regions also tend to $\hat{\psi} > 0$. For both $T_{\rm d}$ and $p_{\rm d}$, the correspondence with regions of lower variance may be related to the signal-to-noise ratio of the misalignment measurement. In regions with higher polarized intensity, there is less variance in $\hat{\psi}$.

There may also be a connection to $S_{\rm d}$, the angle dispersion of the dust polarization, and $S_{\rm H\,I}$, that of the H I polarization template. The former anticorrelates with $p_{\rm d}$; i.e., regions of greater polarization-angle coherence have larger polarization fractions (Planck Collaboration et al. 2020e). The variation in polarization-angle coherence may be related to the magnetic-field orientation relative to the line of sight (e.g., Hensley et al. 2019). The H I-based dispersion $S_{\rm H\,I}$ and polarization fraction $p_{\rm H\,I}$ also anticorrelate, and the alignment of the dust polarization angle to the H I template anticorrelates with $S_{\rm H\,I}$ (Clark & Hensley 2019). We would therefore expect that regions of larger polarization fraction correlate with regions of coherent magnetic misalignment, which is indeed what we observe.

6.5. Large Sky Areas

A major motivation for this study is to understand the origin of the parity-violating *TB* correlation measured by Planck on large fractions of the high-latitude sky (Clark et al. 2021). In addition to measuring the variation in misalignment angle

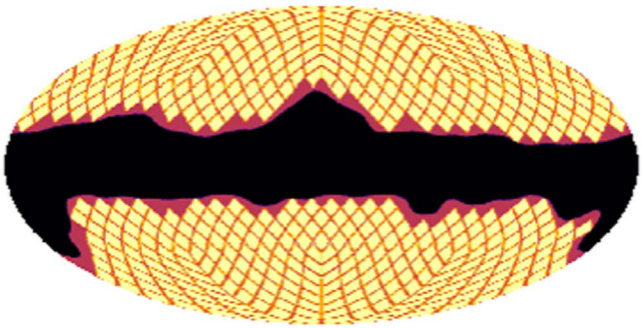

Figure 8. Patches included in the analysis when the masks are defined by $N_{\rm side} = 8$ and an overall 70% Galaxy mask. The red area is allowed by the Galaxy mask, and the yellow patches are those that lie within the red area.

across relatively small patches of sky (Figure 7), we can apply our estimator (Equation (29)) to large sky areas and compare to expectations based on measured cross-spectra (Equation (21)). On large sky areas, the variation in $\hat{\psi}$ is suppressed, and we can safely make a small-angle approximation. Then we expect

$$\hat{\psi}_\ell \approx \frac{D_\ell^{E_{\rm H\,I}B_{\rm d}}}{2D_\ell^{E_{\rm H\,I}E_{\rm d}}} = -\frac{D_\ell^{B_{\rm H\,I}E_{\rm d}}}{2D_\ell^{B_{\rm H\,I}B_{\rm d}}} = \frac{D_\ell^{T_{\rm H\,I}B_{\rm d}}}{2D_\ell^{T_{\rm H\,I}E_{\rm d}}} = \frac{D_\ell^{T_{\rm d}B_{\rm d}}}{2D_\ell^{T_{\rm d}E_{\rm d}}}. \quad (30)$$

Noise in the denominators may bias these expressions, but we are here looking only for a broad consistency and the approximate level of aggregate misalignment on large sky areas. Since $\hat{\psi}_\ell$ is estimated by reference to the H I template, we expect greatest consistency with the dust–H I cross-spectra, e.g., $E_{\rm H\,I}B_{\rm d}$, as opposed to the Planck-only $T_{\rm d}B_{\rm d}$ and $E_{\rm d}B_{\rm d}$.

In Figure 10, we compare the misalignment estimates from Equation (30) for a 70% Galaxy mask (Section 2.1). We find a misalignment angle of $\sim 2^\circ$ that is coherent in the range $101 < \ell < 702$. As expected, $\hat{\psi}$ tends to be more consistent with the dust–H I cross-spectra, especially $E_{\rm H\,I}B_{\rm d}$ and $T_{\rm H\,I}B_{\rm d}$, which are more sensitive than $B_{\rm H\,I}E_{\rm d}$ (Section 4.2). The Planck-only $T_{\rm d}B_{\rm d}$ is more discrepant (though not dramatically so) but reproduces the coherently positive behavior for $\ell < 500$.

The $\hat{\psi}$ estimates are broadly consistent between the northern and southern Galactic hemispheres. In particular, the magnitude of the misalignment and its scale (multipole) independence are consistent. The Planck-only $T_{\rm d}B_{\rm d}/2T_{\rm d}E_{\rm d}$ (red in Figure 10) also shows a similar consistency between the hemispheres. The positive $\hat{\psi}$, the approximate scale independence of $\hat{\psi}$, and the consistency of $\hat{\psi}$ between hemispheres are robust to the choice of Galaxy mask; we checked this for $f_{\rm sky} \in \{40\%, 60\%, 70\%, 80\%, 90\%\}$ (Section 2.1) and present some related results in Section 6.7. The consistency between hemispheres begs for an explanation, which should be a target for future investigations.

The uncertainties on $\hat{\psi}$ in Figure 10 are derived from the scatter of our mock skies (Section 5) and used only for visualization purposes, namely, to give a rough indication of the expected variance. We do not rely on these uncertainties for statistical inference.

Because the large-scale (low-ℓ) modes are difficult to reproduce in our mock-sky framework (Section 5), we have restricted Figure 10 to $101 < \ell < 702$. We can calculate $\hat{\psi}$ for $\ell < 101$, but we cannot form a reliable uncertainty based on mock skies. Nevertheless, it is interesting to report the values for $\hat{\psi}_{\ell<101}$. We find $1\overset{\circ}{.}4$ when using both hemispheres, $2\overset{\circ}{.}9$ in the northern hemisphere, and $0\overset{\circ}{.}7$ in the southern hemisphere. The statistical weight cannot be evaluated in the present analysis, but it is noteworthy that the large scales show the same tendency for misalignment to be positive.

6.6. Aggregate Global Misalignment?

An intriguing possibility is that there is an aggregate global misalignment of $\sim 2^\circ$. An aggregate misalignment would appear as an isotropic, multipole-independent rotation of the dust polarization relative to the filamentary structures, i.e., $\psi_\ell = \text{constant}$. The implied magnetic-field structure relative to the dust intensity field would be qualitatively similar to that depicted by the green pseudovectors in Figure 3. A global polarization rotation can also be produced by a miscalibration of the absolute polarization angle or in the CMB by the phenomenon of cosmic birefringence (Section 1.3).

We consider miscalibration to be unlikely, since Planck estimates a systematic uncertainty of $0\overset{\circ}{.}28$ (Planck Collaboration et al. 2016d), nearly an order of magnitude smaller than our measured misalignment. In the following sections, we measure $\hat{\psi}$ in small sky regions and search for correlated variations with other interesting quantities. The relative variation from region to region is insensitive to an overall miscalibration.

A global misalignment signal in the dust, which acts as a foreground for CMB measurements, would need to be accounted for in searches for cosmic birefringence, especially with methods that rely on the symmetry properties of the dust polarization, e.g., Minami et al. (2019).

As a consistency check, we modified our H I template (Section 3) by imposing a global polarization rotation of 2°. This rotation mixes the E and B modes. Because the H I template is dominated by E modes ($E_{\rm H\,I}E_{\rm H\,I}/B_{\rm H\,I}B_{\rm H\,I} \sim 5$ for $\ell > 100$), the effect is fractionally stronger in the B modes. We can estimate the expected impact of this modification by considering that $2^\circ \approx 0.03$ rad, so this should produce a percent-level change in the correlations. We correlate with the Planck dust maps and find that the B-mode correlation for $100 < \ell < 700$ increases by 0.1%–0.5% in addition to the original correlation of 10%–25%, which is indeed a fractional increase of $\mathcal{O}(1\%)$. We performed the same exercise with the opposite rotation, i.e., by -2°, and we find an approximately symmetric decrease in the H I–Planck correlation. These results are consistent with the estimates of Figure 10 and increase our confidence in a true on-sky aggregate misalignment of approximately 2°.

The $T_{\rm d}B_{\rm d}$-based estimate of ψ_ℓ (red in Figure 10) is coherent only over the range $100 \lesssim \ell \lesssim 500$. Where it is nonzero, it also tends to be larger than $\hat{\psi}$. The discrepancy may be an indication that $T_{\rm d}B_{\rm d}$ and $T_{\rm d}E_{\rm d}$ are affected by additional polarization sources that are missed by the filamentary misalignment model, and it is conceivable that the simultaneous positivity of $T_{\rm d}B_{\rm d}$ and $\hat{\psi}$ is merely coincidental. In Section 8, we seek further evidence of a relationship by analyzing small sky patches.

6.7. Varying Sky Fraction

We track the dependence of these misalignment estimates on the sky fraction $f_{\rm sky}$. In Figure 10, we consider only $f_{\rm sky} = 70\%$, whereas we now allow $f_{\rm sky} \in \{20\%, 40\%, 60\%, 70\%, 80\%, 90\%, 97\%\}$ (Figure 1). In Figure 10, we consider multiple estimators for ψ_ℓ. For simplicity, we now downselect to only two. One is $\psi_\ell^{\rm d\times d} \equiv \text{atan2}(T_{\rm d}B_{\rm d}, T_{\rm d}E_{\rm d})/2$ (red in Figure 10), which uses only the dust field (see Figure 9 of Clark et al. 2021). We contrast the dust-only estimator with one that includes some

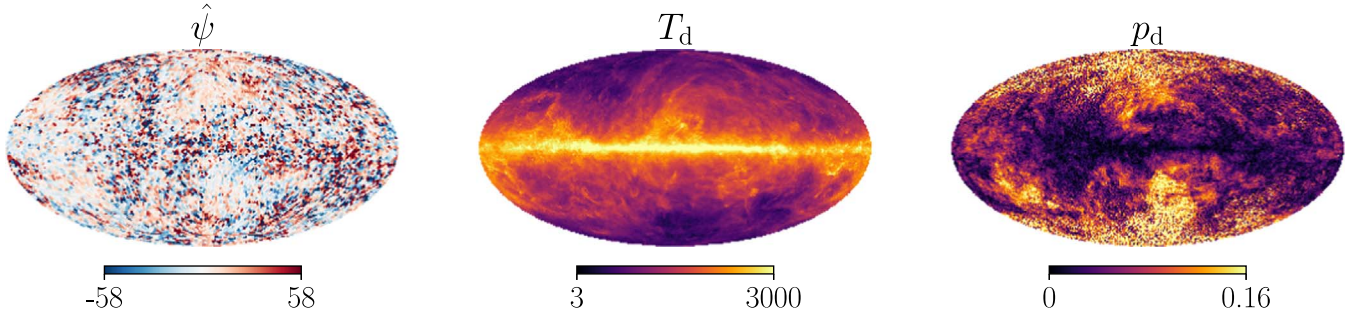

Figure 9. Maps of misalignment angle $\hat{\psi}$ (left), dust intensity $T_{\rm d}$ (middle), and dust polarization fraction $p_{\rm d}$ (right). The $\hat{\psi}$ map has been created with $N_{\rm side} = 32$ and is identical to the bottom left panel of Figure 7. The $T_{\rm d}$ and $p_{\rm d}$ maps are shown after smoothing to the HI4PI beam (16′.2) and downgrading to $N_{\rm side} = 256$. The $\hat{\psi}$ values are in degrees, and dust intensity is in $\mu{\rm K_{RJ}}$. We note the similarities in the large-scale features of $\hat{\psi}$ and $p_{\rm d}$.

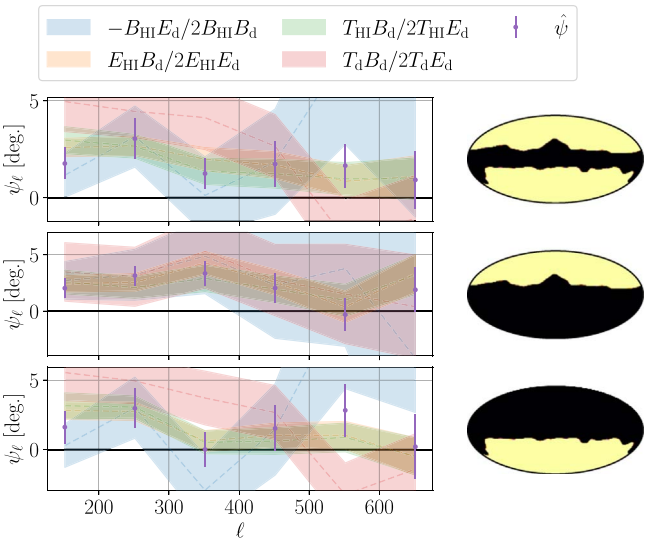

Figure 10. Comparison of misalignment-angle estimates from $\hat{\psi}$ (Equation (29)) and parity-violating cross-spectra (Equation (30)) for a 70% Galaxy mask (Section 2.1) and each hemisphere independently (bottom two rows). The $\hat{\psi}$ estimates are formed after filtering the Planck and H I maps to each multipole bin ($\Delta\ell = 100$). The parity-violating spectra are shown with Gaussian uncertainties. The green and orange bands are nearly identical and difficult to separate visually. The error bars on the $\hat{\psi}$ points are from the standard deviations of our mock skies (Section 5). We find an approximately scale-independent positive $\hat{\psi}$ that persists at the same level in both hemispheres and is broadly consistent with the spectrum-based estimators, especially those incorporating the H I template.

H I filamentary information: $\psi_\ell^{\rm H\,I\times d} \equiv {\rm atan2}(T_{\rm H\,I}B_{\rm d}, T_{\rm H\,I}E_{\rm d})/2$ (green in Figure 10). Whereas $\psi_\ell^{\rm d\times d}$ includes information from the entire dust field, $\psi_\ell^{\rm H\,I\times d}$ collapses the misalignment estimate onto the filamentary modes. When the two are in agreement, the filamentary magnetic misalignment is representative of the parity violation in the full dust field. When they deviate from each other, the H I template may be incomplete or inaccurate, or the full dust field may contain parity-violating contributions that are nonfilamentary.

In Figure 11, we show $\psi_\ell^{\rm d\times d}$ and $\psi_\ell^{\rm H\,I\times d}$ for a variety of sky fractions $f_{\rm sky}$.

We show the estimates for individual multipole bins (see Figure 10), and we also high pass filter to form the broadband $\psi_{\ell>100}$, which may potentially average away signal but is less noisy. We find that $\psi_\ell^{\rm H\,I\times d}$ is consistently positive over all ℓ and remains in the range of 0°–5°, while $\psi_\ell^{\rm d\times d}$ is much more variable, especially at large $f_{\rm sky}$. We note that the two estimates display closer agreement at small $f_{\rm sky}$, i.e., when restricting to high Galactic latitudes. At the same time, we find that $\psi_{\ell>100}^{\rm H\,I\times d}$ steadily decreases from ∼3° to ∼1° as $f_{\rm sky}$ increases from 20% to 97% (right panels of Figure 11), a phenomenon that is observed in both hemispheres independently. The decline may be related to the fact that the H I becomes a less robust tracer of dust at low Galactic latitudes where the column densities are relatively large (e.g., Lenz et al. 2017), so it may be that the H I template is simply less representative of the dust field for large $f_{\rm sky}$.

Interestingly, all of the variations considered in Figure 11 produce $\psi_\ell^{\rm H\,I\times d}$ in the range of 0°–5°. This behavior persists for all of the considered multipoles and sky fractions and in both hemispheres independently. Furthermore, we performed this analysis with the RHT-based H I template (Clark & Hensley 2019; Appendix A.1) instead of the Hessian, and we find consistent results. These observations lend more weight to the speculations of Section 6.6 about a possible global misalignment angle of ∼2°.

7. What is "Magnetic Misalignment"?

While random deviations constitute a form of "misalignment" relative to the H I-defined filaments, it is unsurprising that such deviations are detected. The H I-based polarization templates (presented here and in, e.g., Clark & Hensley 2019) correlate strongly with the Planck dust maps, but they are not identical, even within the limits of the Planck noise. If the term "magnetic misalignment" is to refer to any kind of deviation from the H I template, then a detection of misalignment teaches us only that the H I template is an incomplete description of the dust polarization field.

As a result of these considerations, we focus much of the rest of our analysis on a search for magnetic misalignment that displays certain types of coherence, which is less likely to be mimicked by random deviations from an H I template. We search for coherence in both harmonic and map space. Harmonic coherence indicates that ψ_ℓ is approximately constant with ℓ and manifests as a uniform rotation of the dust polarization pseudovectors relative to the H I predictions (Figure 3). We also refer to harmonic coherence as scale independence.

We restrict the analysis to the high-latitude sky by masking the Galactic plane to varying levels. Our fiducial choice is the Planck 70% Galaxy mask. For example, when dividing the sky into patches defined by pixels with $N_{\rm side} = 8$, we consider only those shown in Figure 8.

In subsequent sections, we will consider other, similarly parameterized Galaxy masks and patch sizes.

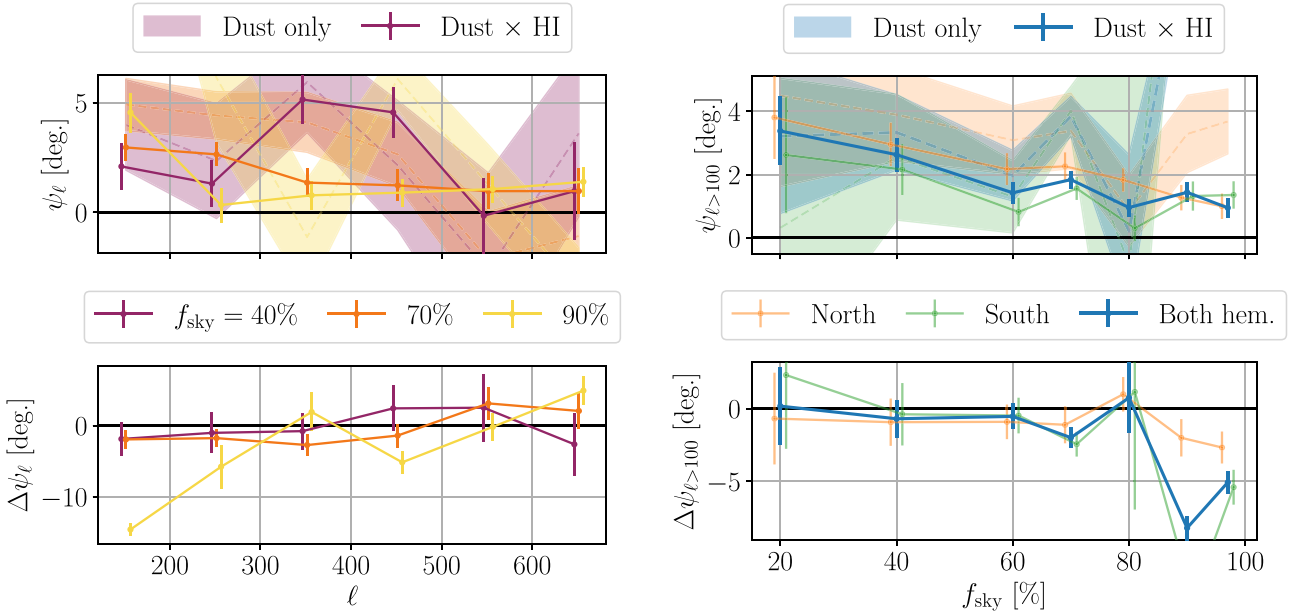

Figure 11. Misalignment estimates $\psi_\ell^{x\times d} = \mathrm{atan2}(T_x B_d,\, T_x E_d)/2$ (Equation (19)) with $x = \mathrm{d}$ ("dust only") and $x = \mathrm{H\,I}$ ("dust × H I") for a varying sky fraction $f_{\rm sky}$. The top panels show the two types of estimates; the bottom panels show the differences.

In Appendix B, we introduce a number of cross-power and correlation metrics, which are used throughout the following sections.

7.1. Harmonic Coherence

The relative constancy of the Planck TB/TE at high latitudes (see, e.g., Figure 9 of Clark et al. 2021) is perhaps a hint that magnetic misalignment, if it is to address the mystery of the positive dust TB, ought to display a harmonic coherence in the multipole range $100 \lesssim \ell \lesssim 500$. Indeed, we find that a direct calculation of the misalignment angle $\hat{\psi}_\ell$ yields an apparent coherence over an even larger multipole range, tentatively across all $\ell < 702$ (Figure 10 and Section 6.5). Is the apparent harmonic coherence an emergent phenomenon that appears only when aggregating large sky areas? In this section, we divide the sky into smaller patches and test whether harmonic coherence is a generic feature of magnetic misalignment.

To look for coherence in harmonic space, we bandpass filter the maps into two disjoint multipole ranges. For all of our results, $101 < \ell < 702$, so $\ell_{\rm min} = 101$ and $\ell_{\rm max} = 702$ can be taken as lower and upper limits, respectively, on the multipole ranges. We form a set of maps with $\ell < \ell_c - \Delta\ell/2$ and a set with $\ell > \ell_c + \Delta\ell/2$, where ℓ_c is a transition multipole and $\Delta\ell$ is a multipole buffer between the two ranges. We allow $\Delta\ell \in \{0, 100, 200\}$, and we sweep ℓ_c across the range [101, 702].

Let $\hat{\psi}_{\rm lo}(\hat{\boldsymbol{n}})$ be the misalignment angle estimated in the patch centered on sky coordinate $\hat{\boldsymbol{n}}$ after filtering to $\ell < \ell_c - \Delta\ell/2$, and let $\hat{\psi}_{\rm hi}(\hat{\boldsymbol{n}})$ be similarly defined after filtering to $\ell > \ell_c + \Delta\ell/2$. We will refer to $\hat{\psi}_{\rm lo}(\hat{\boldsymbol{n}})$ and $\hat{\psi}_{\rm hi}(\hat{\boldsymbol{n}})$, respectively, as the "low-pass-filtered" and "high-pass-filtered" misalignment estimates. Recall, however, the multipole limits $\ell_{\rm min}$ and $\ell_{\rm max}$ mentioned above, so these estimates are, in fact, products of bandpass filtering.

Our correlation calculations must consider the circularity of the misalignment angle. We expect $\hat{\psi}$ to cluster around 0° mod 180°. Even for the smallest masks of Figure 7, which are defined by $N_{\rm side} = 32$, the majority of $\hat{\psi}$ values lie within $[-45°, 45°]$ mod 180°. In our correlations, therefore, we ignore the circularity of $\hat{\psi}$ and instead force the values to their physical equivalents in the range $[-90°, 90°]$. In a small minority of cases, we will miss correlations between angles that lie at opposite extremes of this range. In testing for a correlation, our choice is conservative. Since we will be using Spearman correlations, which operate on rank variables, a convenient ordering strategy is to form $\tan\hat{\psi}$.

We form the Spearman cross-power (Spearman version of Equation (B2))

$$\hat{\psi}_{\rm lo} \times \hat{\psi}_{\rm hi} \equiv s_s(\tan\hat{\psi}_{\rm lo}, \tan\hat{\psi}_{\rm hi}), \tag{31}$$

where the sum is taken over patches labeled by $\hat{\boldsymbol{n}}$. Note that these Spearman cross-powers are not correlation coefficients, so the numerical values range outside of $[-1, 1]$. Correlation coefficients are less numerically stable in the presence of noise, so we prefer cross-powers for the purposes of establishing a relationship. In Figure 12, we show $\hat{\psi}_{\rm lo} \times \hat{\psi}_{\rm hi}$ for several choices of ℓ_c and $\Delta\ell$ for the patches of Figure 8 (masks defined by $N_{\rm side} = 8$ and $f_{\rm sky} = 70\%$). We find a positive cross-power for $\ell_c \lesssim 450$ for all choices of $\Delta\ell$. The noise in these measurements is mainly in the high-pass-filtered misalignment estimates $\hat{\psi}_{\rm hi}$.

We do not expect our mock skies (Section 5) to show a coherence over ℓ because the Gaussian modes are resampled independently of each other and the H I template. One concern might be that the masking creates mode correlations, and this was part of the motivation for introducing the multipole buffer $\Delta\ell$. As $\Delta\ell$ increases, the two multipole passbands are further separated, and spurious correlations between the two are less likely.

As a null test, we calculate $\hat{\psi}_{\rm lo} \times \hat{\psi}_{\rm hi}$ for an ensemble of mock skies (Section 5), and we find the mean values to be consistent with zero. Recall that these mock skies are simplified in the sense that they are designed to reproduce only the two-point statistics of the dust field, both in correlation with itself and with the H I template. Nonetheless, they are helpful in

checking that our estimators produce sensible results. The H I template appears in these mock skies with the observed amplitude, and the only magnetic misalignment that has been input is due to random scatter. We see no positive bias in the mock-sky cross-powers. The positive signal seen in the real map (Figure 12) must be due to a feature that it is absent in the mock skies.

Due to noise in the $\hat{\psi}$ estimates, it is nontrivial to determine the fraction of the misalignment signal that is harmonically coherent. In computing a correlation coefficient, noise tends to dilute the true signal. Using half-mission splits as in Equation (B3) may lead to numerical pathologies when the denominators are small. From the decay of $\hat{\psi}_{\rm hi}^{(1)} \times \hat{\psi}_{\rm hi}^{(2)}$ in Figure 12, we see that the high-pass-filtered estimate $\hat{\psi}_{\rm hi}$ is especially noisy. The Spearman cross-powers $\hat{\psi}_{\rm lo}^{(1)} \times \hat{\psi}_{\rm lo}^{(2)}$ (red in Figure 12) and $\hat{\psi}_{\rm hi}^{(1)} \times \hat{\psi}_{\rm hi}^{(2)}$ (purple) are limited only by noise and set rough upper limits on the cross-power $\hat{\psi}_{\rm lo} \times \hat{\psi}_{\rm hi}$. Even if the misalignment angles were perfectly coherent across multipoles, noise would suppress the cross-power. That $\hat{\psi}_{\rm lo} \times \hat{\psi}_{\rm hi}$ is of the same order as $\hat{\psi}_{\rm lo}^{(1)} \times \hat{\psi}_{\rm lo}^{(2)}$ and $\hat{\psi}_{\rm hi}^{(1)} \times \hat{\psi}_{\rm hi}^{(2)}$ is an indication that, within the limits of the noise, the harmonically coherent component is contributing a nonnegligible fraction of the misalignment signal.

We estimate the statistical significance of the apparently positive signal in Figure 12. For each choice of $\ell_{\rm c}$ and $\Delta\ell$, we construct permutation tests (Appendix B.1), where covariances are preserved by using the same permutations for all choices. We combine the results with weights based on the half-mission cross-powers (bands in Figure 12) and produce a single overall estimate of the statistical significance. For the case of Figure 12, we estimate the statistical significance to be 2.3σ, where most of the sensitivity comes from the cross-powers with smaller $\ell_{\rm c}$ and smaller $\Delta\ell$. This is because $\hat{\psi}_{\rm hi}$ quickly becomes noise-dominated as $\ell_{\rm c}$ increases, and increasing $\Delta\ell$ pushes the filter cutoff even higher. The data points in Figure 12 are computed from the same maps but with different filtering parameters, so we expect them to be highly correlated. As such, combining the data points increases the overall significance only modestly. To a rough approximation, the overall significance can be estimated from the lowest-$\ell_{\rm c}$ data point.

The results of Figure 12 are based on the patches shown in Figure 8, which are defined by $N_{\rm side} = 8$ and $f_{\rm sky} = 70\%$. We can compute similar quantities for other values of $N_{\rm side}$ and $f_{\rm sky}$, and the results are compiled in Table 1, where we see that the significances are generally between 2σ and 4σ for $N_{\rm side} \in \{2, 4, 8, 16, 32\}$ and $f_{\rm sky} \in [60\%, 90\%]$. With smaller $f_{\rm sky}$, the significances tend to be smaller, but this may be simply a consequence of a decreased signal-to-noise ratio. On the full sky, the significances also tend to decrease, and this may be due to the inclusion of longer, denser sight lines at low Galactic latitudes. We do not attempt to combine the results from different choices of $N_{\rm side}$ and $f_{\rm sky}$ because the covariances are difficult to capture.

We consider the results of Figure 12 and Table 1 to represent tentative evidence for the harmonic-space coherence of misalignment angles measured in small regions of sky away from the Galactic plane.

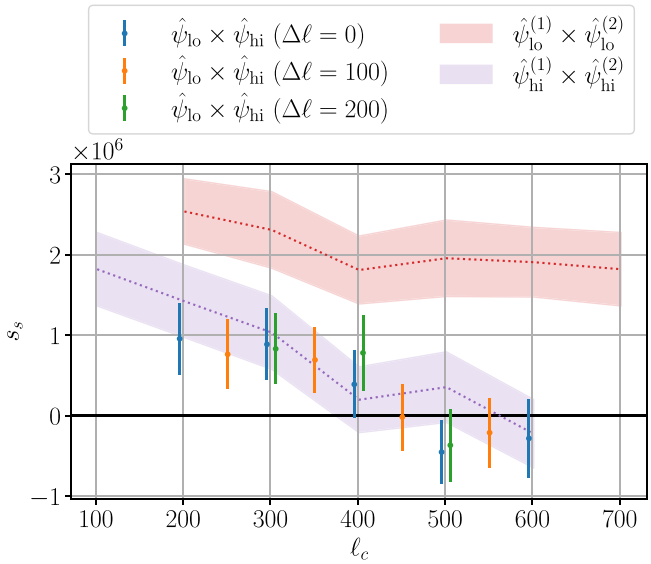

Figure 12. Cross-power s_s between misalignment angles estimated from low- and high-pass-filtered maps (Equation (31)): $\hat{\psi}_{\rm lo} \times \hat{\psi}_{\rm hi}$ for the patches of Figure 8. We consider three values for $\Delta\ell$, and the data points have been offset from $\ell_{\rm c}$ for visual purposes. We also show the cross-power between half-mission splits in the shaded bands for low- ($\hat{\psi}_{\rm lo}^{(1)} \times \hat{\psi}_{\rm lo}^{(2)}$) and high- ($\hat{\psi}_{\rm hi}^{(1)} \times \hat{\psi}_{\rm hi}^{(2)}$) pass-filtered estimates. The $\hat{\psi}_{\rm hi}$ estimates become noise-dominated for $\ell_c \gtrsim 400$. This is a test for the harmonic coherence (scale independence) of magnetic misalignment, and we find a positive signal for $\ell_c \lesssim 450$.

Table 1
Statistical Significance (in Units of σ) of Measurements of the Harmonic Coherence of $\hat{\psi}$, e.g., Those Presented in Figure 12, for Different Values of $N_{\rm side}$ (Rows with Side Lengths Provided Parenthetically) and $f_{\rm sky}$ (Columns)

	40%	60%	70%	80%	90%	100%
2 (29.°3)	1.1	2.6	3.0	3.8	3.6	0.2
4 (14.°7)	3.7	3.3	3.5	3.2	2.8	0.9
8 (7.°3)	1.9	2.4	2.3	2.5	3.9	3.1
16 (3.°7)	1.2	2.8	2.7	3.3	2.2	2.2
32 (1.°8)	3.8	3.9	4.2	2.5	1.5	1.1

Note. All of the results are positive with little dependence on $N_{\rm side}$ and $f_{\rm sky}$.

7.2. Spatial Coherence

We additionally search for spatial coherence of misalignment angles by considering neighboring pairs of sky masks. Although we bandpass-filtered to $101 < \ell < 702$ in order to include only modes with wavelengths smaller than each patch, there is still a residual correlation between neighboring patches, which we detect with the mock skies of Section 5. To avoid the coherence due to common modes between neighboring patches, we again construct high- and low-pass-filtered maps as in Section 7.1. We correlate the low-pass-filtered estimate from each patch with the high-pass-filtered estimate from each of its neighbors, and we simultaneously correlate with the opposite application of filters. The misalignment estimates that enter the correlation calculations are separated in both harmonic and map space.

We utilize the Spearman version of the four-variable cross-power (Equation (B5))

$$\hat{\psi}_{\rm lo}(\hat{\boldsymbol{n}}) \times \hat{\psi}_{\rm hi}(\hat{\boldsymbol{n}}') \equiv S_s(\tan\hat{\psi}_{\rm lo}(\hat{\boldsymbol{n}}), \tan\hat{\psi}_{\rm hi}(\hat{\boldsymbol{n}}'), \tan\hat{\psi}_{\rm hi}(\hat{\boldsymbol{n}}), \tan\hat{\psi}_{\rm lo}(\hat{\boldsymbol{n}}'), \quad (32)$$

where $\hat{\boldsymbol{n}}$ and $\hat{\boldsymbol{n}}'$ are the central sky coordinates of neighboring patches. As in Section 7.1, we consider several choices for $N_{\rm side}$ and $f_{\rm sky}$, where Figure 8 shows one example. The sum is taken over all pairs of neighboring patches. Each patch appears multiple times in this sum, but each pair appears only once. Equation (32) measures a simultaneous correlation between $\hat{\psi}_{\rm lo}(\hat{\boldsymbol{n}})$ and $\hat{\psi}_{\rm hi}(\hat{\boldsymbol{n}}')$ and between $\hat{\psi}_{\rm hi}(\hat{\boldsymbol{n}})$ and $\hat{\psi}_{\rm lo}(\hat{\boldsymbol{n}}')$. The entire multipole range is being used in both patches but in two splits. Without multipole separation, we cannot pass a null test based on our mock skies (Section 5). With multipole separation, however, the mock skies show no significant cross-power.

The results for $\hat{\psi}_{\rm lo}(\hat{\boldsymbol{n}}) \times \hat{\psi}_{\rm hi}(\hat{\boldsymbol{n}}')$ (Equation (32)) are shown in Figure 13 for patches defined by $N_{\rm side} = 16$. This patch area is four times smaller than that used for the measurement of harmonic coherence (Figure 12). Measuring neighbor correlations at $N_{\rm side} = 16$ probes the spatial coherence within patches defined by $N_{\rm side} = 8$, so we are approximately measuring the spatial coherence within the patches of Figure 12. For the particular example of Figure 13, we find positive spatial coherence for $\ell_c \lesssim 500$.

We estimate the statistical significance of the positive signal shown in Figure 13 by following a prescription similar to that of Section 7.1. Combining all of the measurements in a manner that accounts for covariances, we estimate the statistical significance to be 3.6σ, where most of the sensitivity, as for harmonic coherence, comes from the low-ℓ_c, low-$\Delta\ell$ cross-powers.

We can compute similar quantities with other values of $N_{\rm side}$ and $f_{\rm sky}$, and the results are compiled in Table 2, where we see that the spatial coherence tends to be stronger as the resolution is made finer.

For $N_{\rm side} \in \{16, 32\}$, the significances are mostly between 2σ and 5σ. As the side length associated with $N_{\rm side} = 32$ is $1.^\circ8$, these results may imply that magnetic misalignment displays a coherence length of $\mathcal{O}(1^\circ)$.

We consider the results of Figure 13 and Table 2 to represent tentative evidence for spatial coherence of misalignment angles. One perspective, however, is to consider the spatial coherence to be a necessary implication of the harmonic coherence that was established in Section 7.1. We explained at the beginning of this section that the multipole split in Equation (32) helps to evade correlations between neighboring patches, which appear even in our statistically aligned mock skies (Section 5). The claim is that $\hat{\psi}_{\rm lo}(\hat{\boldsymbol{n}})$ is correlated with $\hat{\psi}_{\rm lo}(\hat{\boldsymbol{n}}')$ even in the mock skies. So we chose to correlate $\hat{\psi}_{\rm lo}(\hat{\boldsymbol{n}})$ with $\hat{\psi}_{\rm hi}(\hat{\boldsymbol{n}}')$, and the mock skies show no correlation in this case. But the mock skies are also lacking harmonic coherence. In the real maps, harmonic coherence appears to correlate $\hat{\psi}_{\rm lo}(\hat{\boldsymbol{n}})$ with $\hat{\psi}_{\rm hi}(\hat{\boldsymbol{n}})$ and $\hat{\psi}_{\rm lo}(\hat{\boldsymbol{n}}')$ with $\hat{\psi}_{\rm hi}(\hat{\boldsymbol{n}}')$ (Section 7.1), but then we should expect, on the basis of the residual neighbor-to-neighbor correlations in the mock skies, a correlation between $\hat{\psi}_{\rm lo}(\hat{\boldsymbol{n}})$ and $\hat{\psi}_{\rm hi}(\hat{\boldsymbol{n}}')$ and between $\hat{\psi}_{\rm hi}(\hat{\boldsymbol{n}})$ and $\hat{\psi}_{\rm lo}(\hat{\boldsymbol{n}}')$. So there may indeed be a spatial coherence, but the crucial ingredient might be the harmonic coherence.

8. Parity-violating Cross-spectra

We now investigate connections between the misalignment angle $\hat{\psi}$ and the parity-violating cross-spectra $T_{\rm d}B_{\rm d}$, $E_{\rm d}B_{\rm d}$, $T_{\rm H\,I}B_{\rm d}$, $E_{\rm H\,I}B_{\rm d}$, and $B_{\rm H\,I}E_{\rm d}$. In Sections 4 and 6.5, we describe the expected relationships. In Figures 4 and 10, we test the implications of these relationships on relatively large sky areas. In those particular cases, we used a 70% Galaxy mask and also checked the robustness of the results by restricting to the northern and southern hemispheres separately.

We now consider finer masks to search for coordinated variation in misalignment angle and parity-violating cross-spectra.

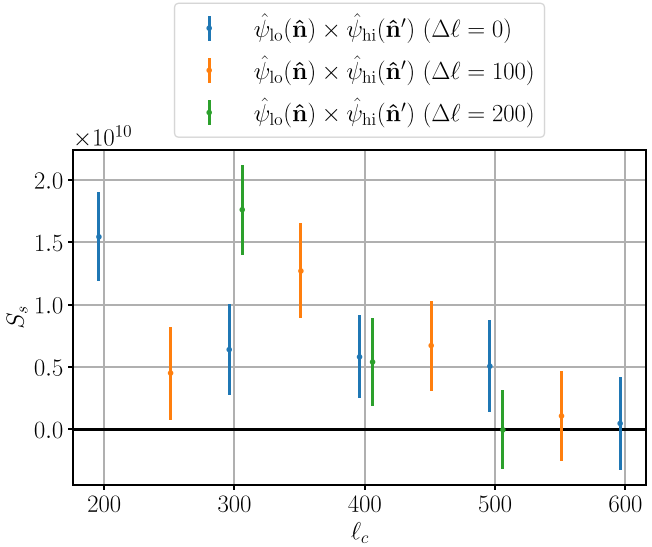

Figure 13. Cross-power S_s (Equation (32)) between misalignment estimates from neighboring patches defined by $N_{\rm side} = 16$ and $f_{\rm sky} = 70\%$. This cross-power splits the misalignment estimates in both harmonic and map space and is a test for spatial coherence. The plotting conventions are the same as in Figure 12. We find a positive signal for $\ell_c \lesssim 500$.

Table 2
Statistical Significance (in Units of σ) of Measurements of the Spatial Coherence of $\hat{\psi}$ (Equation (32)), e.g., Those Presented in Figure 13, for Different Values of $N_{\rm side}$ (Rows with Side Lengths Provided Parenthetically) and $f_{\rm sky}$ (Columns)

	40%	60%	70%	80%	90%	100%
2 ($29.^\circ3$)	−0.1	−2.0	−2.4	−1.0	−0.3	−2.2
4 ($14.^\circ7$)	2.9	1.7	1.8	1.7	2.0	−0.4
8 ($7.^\circ3$)	1.3	0.8	1.0	0.5	0.0	−0.7
16 ($3.^\circ7$)	3.8	3.9	3.6	3.0	2.7	3.4
32 ($1.^\circ8$)	2.9	2.9	4.0	5.1	4.7	4.1

Note. The significances are mostly positive and tend to increase with $N_{\rm side}$.

8.1. Random versus Harmonically Coherent Misalignment

As described in Section 7, we are interested in distinguishing between random and harmonically coherent misalignment. In both cases, we expect to find that the misalignment angle is correlated with *TB* and *EB*, but we can impose additional constraints to isolate harmonically coherent correlations.

Random misalignment is exemplified by the mock skies of Section 5. The mock skies show deviations from the H I template, but the deviations are incoherent across multipoles, and there is no aggregate misalignment on large sky areas (see Section 6.5). We find that the mock skies show significant correlations between $\hat{\psi}_\ell$ and $D_\ell^{T_{\rm d}B_{\rm d}}$ and between $\hat{\psi}_\ell$ and $D_\ell^{E_{\rm d}B_{\rm d}}$. If

we instead correlate between disjoint multipole bins, e.g., $\hat{\psi}_{\ell<\ell_c}$ with $D_{\ell>\ell_c}^{T_dB_d}$ for some cutoff multipole ℓ_c, we find that the correlations vanish. The real data, as we will show in Sections 8.3 and 8.4, display both types of correlations.

The mock skies display correlations between $\hat{\psi}_\ell$ and $D_\ell^{T_dB_d}$ and between $\hat{\psi}_\ell$ and $D_\ell^{E_dB_d}$ as a direct consequence of the known strong correlation between the Planck dust maps and the H I templates (e.g., Clark & Hensley 2019). The H I–dust correlation is maintained in the mock skies. The H I component contributes nonnegligibly to the dust polarization, and the Planck maps can be viewed as perturbed versions of the H I templates. From Figure 6, we see that the perturbations need not be especially small; in fact, the Gaussian-dust component dominates over the H I component, though only modestly. If the perturbations are random, the dust polarization angles are symmetrically distributed relative to the H I template, and $\hat{\psi} = 0$. If, however, there is a region of sky in which the dust polarization angles are distributed asymmetrically relative to the H I template, then $\hat{\psi} \neq 0$; in this case, there will be a net chirality, which will in turn produce nonzero contributions to T_dB_d and E_dB_d. Even in the mock skies, there are regions of sky that fluctuate to nonzero $\hat{\psi}$, and these regions tend to contribute nonzero T_dB_d and E_dB_d with a corresponding sign. Our estimators avoid noise biases, so the relevant fluctuations are likely due to on-sky dust components that deviate from the H I template. This is the expected contribution of magnetic misalignment to the parity-violating dust polarization quantities, but we aim to investigate whether the observed T_dB_d and E_dB_d are consistent with random fluctuations away from the filament orientations—as exemplified by the mock skies—or show evidence for harmonic or spatial coherence, which might be expected from a physical misalignment between the magnetic field and dusty filaments.

It is important to note that, while $\hat{\psi} > 0$ implies a tendency toward T_dB_d, $E_dB_d > 0$, the converse is not guaranteed. It is possible to have T_dB_d, $E_dB_d > 0$ but $\hat{\psi} = 0$. Our mock skies (Section 5) illustrate this point. They are constructed to retain the T_dB_d spectrum of the true dust maps, but this property is placed entirely in the Gaussian component, which is statistically independent of the H I component. As such, the mock skies display no aggregate misalignment (beyond realization-dependent scatter). For example, on a 70% Galaxy mask, the ensemble mean of $\hat{\psi}$ is zero, although the mean T_SB_S spectrum is positive for $100 \lesssim \ell \lesssim 500$, as for the true T_dB_d (Section 1.1).

To the extent that the observed T_dB_d is related to magnetic misalignment, an outstanding question is whether the real dust *TB* is a consequence of physical misalignment or random scatter. Thus, we search for harmonically coherent relationships between misalignment angle and parity-violating cross-spectra. The mock skies will help us to make the distinction, since harmonic coherence is not included in them.

8.2. *Misalignment Controls* TB

We begin the investigation with sky areas that are only modestly smaller than those of Sections 4 and 6.5. In this limit, the aggregate misalignment angles are small, and the expected relationship to parity-violating cross-spectra can be approximated as (see Equation (30))

$$\hat{\psi} \approx \frac{D_\ell^{T_dB_d}}{2D_\ell^{T_dE_d}} \approx \frac{D_\ell^{E_dB_d}}{2(D_\ell^{E_dE_d} - D_\ell^{B_dB_d})}. \quad (33)$$

We will focus more on the dust-only spectra T_dB_d and E_dB_d, as opposed to the dust–H I spectra $T_{H\,I}B_d$, $E_{H\,I}B_d$, and $B_{H\,I}E_d$, but similar operations can be performed for either set.

We divide the sky into patches defined by $N_{side} = 2$ within an overall 70% Galaxy mask. In each patch, we measure $\hat{\psi}$ as in Figure 7 (with an additionally imposed Galaxy mask). We form a combined mask from the patches with $\hat{\psi}$ larger than the median value, and we form an analogous mask for the patches with $\hat{\psi}$ smaller than the median; the masks are shown in the bottom right of Figure 14, where the input $\hat{\psi}$ values are from maps that have been filtered to $101 < \ell < 702$ (as in the right column of Figure 7). We repeat for maps that have been low-pass-filtered to $101 < \ell < \ell_c$ (which will be labeled by the subscript "lo") and for maps that have been high-pass-filtered to $\ell_c < \ell < 702$ (subscript "hi") for $\ell_c \in \{202, 302, 402\}$.

We calculate auto- and cross-spectra for the full combination of patches for the large- and small-$\hat{\psi}$ samples. To avoid sharp mask features at shared vertices of the `HEALPix`-defined patches, we use a conservative apodization scale of 5° for the results in this subsection. Note that, due to the `HEALPix` pixelization and the increased apodization scale, the full combination of patches represents a smaller overall sky area than produced by the fiducial 70% Galaxy mask of Sections 4 and 6.5. The reduction is somewhat severe and leaves a sky fraction of only 37%.

We convert the auto- and cross-spectra to misalignment estimates according to Equation (33). The results are shown in the panel of spectra in Figure 14.

We find that the T_dB_d- and E_dB_d-based misalignment estimates increase and decrease in a manner consistent with the $\hat{\psi}$-based mask definition. The large-$\hat{\psi}$ masks tend to produce larger T_dB_d/T_dE_d and $E_dB_d/(E_dE_d - B_dB_d)$, though the latter is much noisier. The small-$\hat{\psi}$ masks tend to produce smaller spectrum-based estimates; interestingly, the resulting T_dB_d/T_dE_d (blue in the top row of Figure 14) is broadly consistent with zero rather than negative. This may suggest that the positive T_dB_d measured at high Galactic latitudes is due to a few regions of sky with positive misalignment and that the rest of the sky respects parity.

When $\hat{\psi}$ is estimated over the same multipole range as the spectra, as in the leftmost column of Figure 14, we cannot distinguish between the case of random fluctuations and that of harmonically coherent misalignment (Section 8.1). To isolate the harmonically coherent signal, we compare estimates from disjoint multipole ranges as in Sections 7.1 and 7.2. The three rightmost columns Figure 14 show the results when estimating $\hat{\psi}$ from restricted multipole ranges. Because the dust is brighter at low multipoles, the selections based on $\hat{\psi}_{lo}$ tend to be similar to those based on the unfiltered $\hat{\psi}$. For T_dB_d and E_dB_d to respond to the $\hat{\psi}$ selection in the disjoint multipole range is an indication of the harmonic coherence of magnetic misalignment, which was demonstrated in Section 7.1 but has now been explicitly connected to T_dB_d. With multipole splits, the data are too noisy to make a confident claim about E_dB_d. The T_dB_d results, which are less vulnerable to noise fluctuations, are similar for all choices of multipole filtering; furthermore, the small-$\hat{\psi}_{lo}$ and small-$\hat{\psi}_{hi}$ results tend to track each other, as do the large-$\hat{\psi}_{lo}$ and large-$\hat{\psi}_{hi}$ results. This may be yet another indication of the harmonic coherence of $\hat{\psi}$; i.e., the $\hat{\psi}$-based patch selections are broadly similar in all multipole ranges.

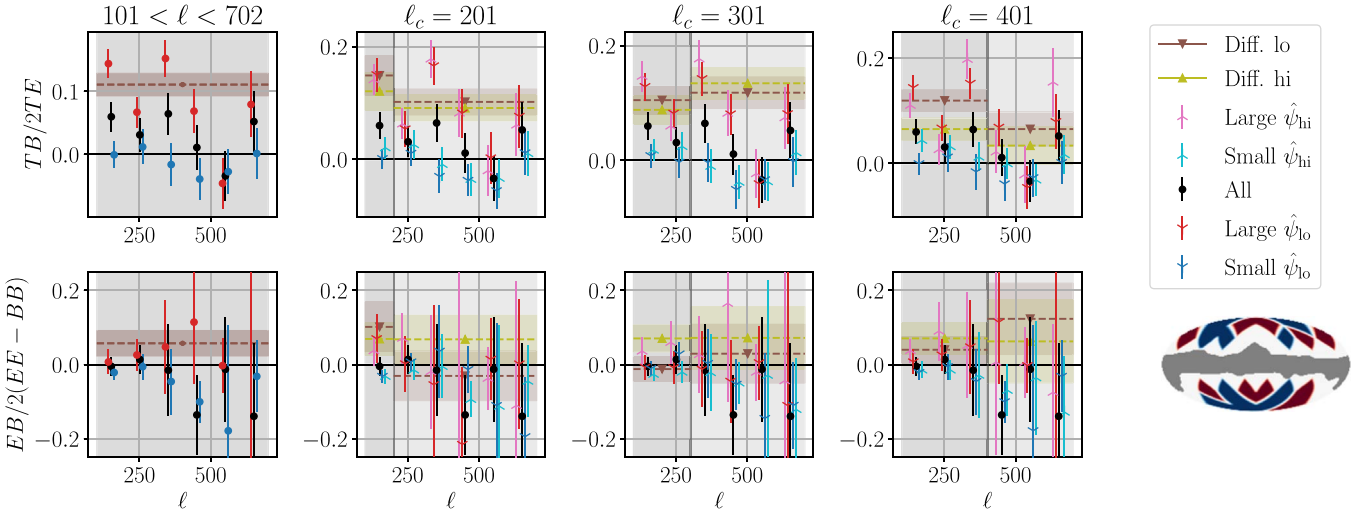

Figure 14. Spectrum-based misalignment estimates (Equation (33)) of $T_{\rm d}B_{\rm d}$ (top row) and $E_{\rm d}B_{\rm d}$ (bottom row) for masks constructed by combining patches selected based on the value of $\hat{\psi}$. In general, we see an increase in the spectrum-based misalignment estimates for large-$\hat{\psi}$ masks and a decrease for small-$\hat{\psi}$. Black points are for the total patch collection (combined red and blue in the bottom right map) and are the same across each row. Red points are from large-$\hat{\psi}$ selections, and blue are from small-$\hat{\psi}$. The leftmost column shows the results from filtering to $101 < \ell < 702$. In the remaining columns, the patch selections are based on $\hat{\psi}_{\rm lo}$, computed after low pass filtering to $101 < \ell < \ell_c$ (darker colors and downward markers), or $\hat{\psi}_{\rm hi}$, computed after high pass filtering to $\ell_c < \ell < 702$ (lighter colors and upward markers), and the background shaded regions indicate the multipole splits. The brown band shows the binned difference between the large- and small-$\hat{\psi}_{\rm lo}$ estimates; yellow shows the same for $\hat{\psi}_{\rm hi}$. (Bottom right) Patch selection based on $\hat{\psi}$ after filtering to $101 < \ell < 702$. Large-$\hat{\psi}$ patches are in red, and small-$\hat{\psi}$ are in blue. The underlying white region is our fiducial 70% Galaxy mask.

We estimate the statistical significance of the multipole-split results by making random patch selections to define the masks. We preserve the covariances by using the same randomization for all $\ell_{\rm c}$. In combining the results from all $\ell_{\rm c}$, we weight by a measure of signal-to-noise ratio (see Section 7.1), and we estimate the overall significance of the harmonic coherence to be 2.2σ for $T_{\rm d}B_{\rm d}$ and 0.8σ for $E_{\rm d}B_{\rm d}$.

8.3. Correlations with Misalignment Angle

We search for correlations between the misalignment angle $\hat{\psi}$ and the parity-violating cross-spectra $T_{\rm d}B_{\rm d}$, $E_{\rm d}B_{\rm d}$, $T_{\rm H\,I}B_{\rm d}$, $E_{\rm H\,I}B_{\rm d}$, and $B_{\rm H\,I}E_{\rm d}$. We outlined our expectations in Equations (17)–(20). For small angles, $\hat{\psi}_\ell$ is expected to track the parity-violating cross-spectra, but there are additional scaling factors. Rather than correlating the spectra with $\hat{\psi}_\ell$ directly, we transform $\hat{\psi}_\ell$ according to Equations (17)–(20).

We compute Spearman half-mission correlation coefficients (see Equation (B4)) because both variables entering each of the following calculations are derived from the same Planck dust modes and therefore subject to covariant noise fluctuations. Due to the aforementioned transformations, the variables are different for each correlation calculation. We compute (see Equations (17)–(20))

$$\tilde{r}_s^{\rm (HM)}\left(D_\ell^{E_{\rm H\,I}B_{\rm d}},\, D_\ell^{E_{\rm H\,I}E_{\rm d}} \tan\left(2\hat{\psi}_\ell\right)\right), \tag{34}$$

$$\tilde{r}_s^{\rm (HM)}\left(D_\ell^{B_{\rm H\,I}E_{\rm d}},\, D_\ell^{B_{\rm H\,I}B_{\rm d}} \tan\left(2\hat{\psi}_\ell\right)\right), \tag{35}$$

$$\tilde{r}_s^{\rm (HM)}\left(D_\ell^{T_xB_{\rm d}},\, D_\ell^{T_xE_{\rm d}} \tan\left(2\hat{\psi}_\ell\right)\right) \tag{36}$$

for $x \in \{{\rm d},\, {\rm H\,I}\}$ and

$$\tilde{r}_s^{\rm (HM)}\left(D_\ell^{E_{\rm d}B_{\rm d}},\, \left(D_\ell^{E_{\rm d}E_{\rm d}} - D_\ell^{B_{\rm d}B_{\rm d}}\right) \tan\left(4\hat{\psi}_\ell\right)\right), \tag{37}$$

where Equation (35) is expected to be negative and all others positive. We show these correlations and maps of the parity-violating quantities in Figure 15 for patches defined by $N_{\rm side} = 8$ (as in Figure 8). The correlations have the expected sign in all cases.

Half-mission cross-correlations (Equation (B4)) avoid noise covariance but not sample variance in the dust measurements. The map features that produce positive $\hat{\psi}$ also produce positive $T_{\rm d}B_{\rm d}$, $E_{\rm d}B_{\rm d}$, $T_{\rm H\,I}B_{\rm d}$, and $E_{\rm H\,I}B_{\rm d}$ and negative $B_{\rm H\,I}E_{\rm d}$ (Section 8.1). While the effective mode weighting in calculating $\hat{\psi}_\ell$ is different than in the cross-spectra, we nevertheless find a correlation between the two in our mock skies (Section 5), for which the non-H I component is statistically independent of the H I component. In particular, the mock skies approximately reproduce the results of Figure 15.

That our mock skies show correlations between misalignment angle and parity-violating cross-spectra is an indication that the correlations of Figure 15 could be attributed to random fluctuations away from the H I template (Section 8.1). This is yet another motivation to restrict the search to signals that are coherent in either harmonic or map space rather than correlating identical patches with identical multipole bins.

Independent of the distinction between random and harmonically coherent misalignment, the correlations of Figure 15 disfavor the presence of significant confounding contributions to parity violation in the polarization field. A priori, we might have expected nonfilamentary contributions to dilute the relationship between H I-based misalignment angle and parity-violating cross-spectra, especially when we consider that the H I-correlated component is a minority contributor to the dust field (Figure 6). Results like those of Figure 15 and the leftmost panel of Figure 14 suggest that the H I template is sufficiently significant and representative to provide a reference for searches for parity violation.

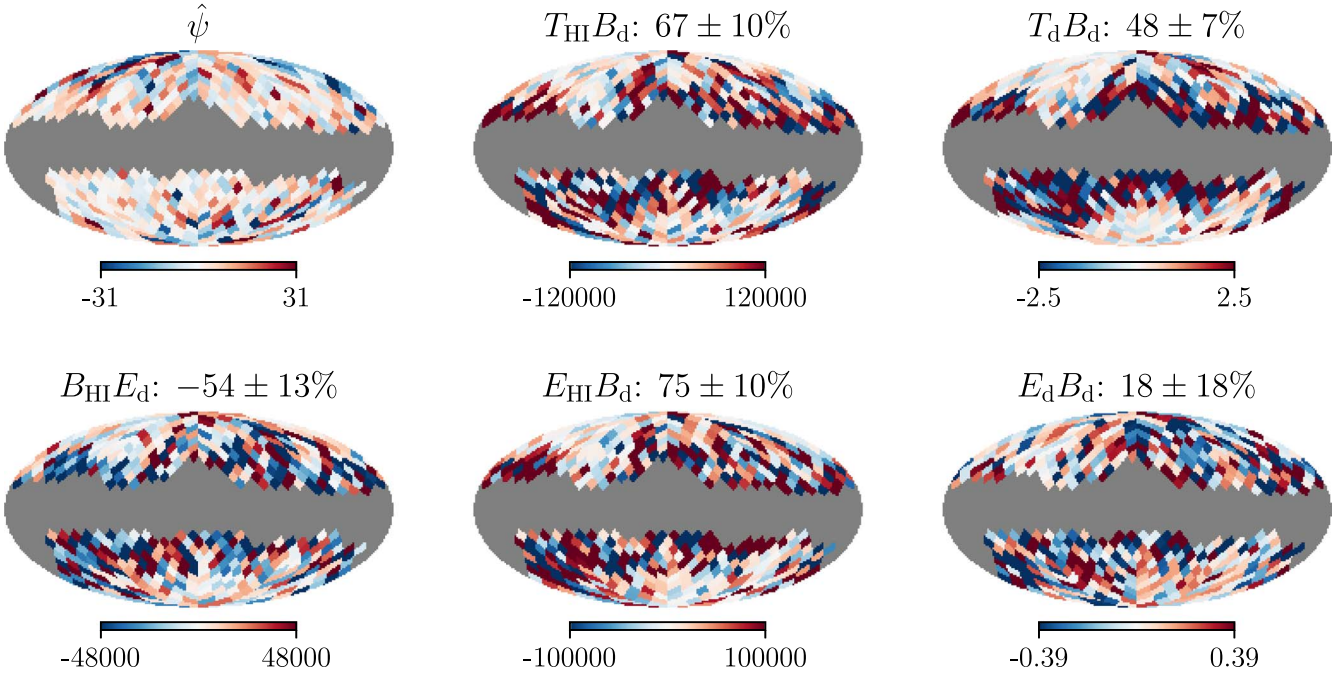

Figure 15. Maps of misalignment angle $\hat{\psi}$ and the five parity-violating cross-spectra binned to $101 < \ell < 702$ for patches defined by $N_{\rm side} = 8$ and $f_{\rm sky} = 70\%$. For $\hat{\psi}$, the units are degrees; for $T_{\rm d}B_{\rm d}$ and $E_{\rm d}B_{\rm d}$, $\mu{\rm K}_{\rm RJ}^2$; and for $T_{\rm H\,I}B_{\rm d}$, $E_{\rm H\,I}B_{\rm d}$, and $B_{\rm H\,I}E_{\rm d}$, $\mu{\rm K}_{\rm RJ}$ K km s^{-1}. For the cross-spectra, the correlation with the transformed $\hat{\psi}$ (Equations (34)–(37)) is given in the subtitle with a 1σ uncertainty (Appendix B.1). We find all of the correlations predicted by the misalignment ansatz (Equations (17)–(20)).

8.4. Harmonic Coherence of Parity Violation

Instead of directly correlating $\hat{\psi}_\ell$ with, e.g., $D_\ell^{T_{\rm d}B_{\rm d}}$, we define disjoint multipole ranges and correlate the low-pass-filtered quantities with the high-pass-filtered. This is similar to the multipole splits described in Section 7.1 and better extracts a signal that is coherent across multipoles. For the misalignment angle, we low or high pass filter the map to form $\hat{\psi}_{\rm lo}$ or $\hat{\psi}_{\rm hi}$, respectively. For the spectra, we simply bin the lower or higher multipoles to form $D_{\rm lo}^{XY}$ or $D_{\rm hi}^{XY}$, respectively. As in Section 7.1, the low-pass-filtered multipole range is $101 < \ell < \ell_c - \Delta\ell/2$, and the high-pass-filtered is $\ell_c + \Delta\ell/2 < \ell < 702$, where $\ell_{\rm c}$ is a transition multipole, and $\Delta\ell$ is a multipole buffer between the two ranges.

We now modify Equations (34)–(37) to correlate across multipole splits. We filter the spectra in the same way and the misalignment angle in the opposite way; e.g., we correlate $D_{\rm lo}^{T_{\rm d}B_{\rm d}}$ with $D_{\rm lo}^{T_{\rm d}E_{\rm d}}\tan(2\hat{\psi}_{\rm hi})$. We are seeking a relationship between $D_{\rm lo}^{T_{\rm d}B_{\rm d}}$ and $D_{\rm lo}^{T_{\rm d}E_{\rm d}}$, and our hypothesis is that the connection is provided by $\hat{\psi}_{\rm hi}$, even though the latter is estimated in a disjoint multipole range. We look for a simultaneous correlation when the multipole ranges are switched.

For this purpose, we use the Spearman version of the four-variable cross-power (Equation (B5))

$$\hat{\psi} \times T_{\rm d}B_{\rm d} \equiv S_s(D_{\rm lo}^{T_{\rm d}B_{\rm d}}, D_{\rm lo}^{T_{\rm d}E_{\rm d}}\tan(2\hat{\psi}_{\rm hi}), D_{\rm hi}^{T_{\rm d}B_{\rm d}}, D_{\rm hi}^{T_{\rm d}E_{\rm d}}\tan(2\hat{\psi}_{\rm lo})) \quad (38)$$

and similar combinations for the other four parity-violating cross-spectra. The cross-powers are presented in Figure 16 for patches defined by $N_{\rm side} = 8$ (as in Figure 8). We also form these cross-powers for an ensemble of mock skies. As noted earlier, our mock skies cannot be used for null-hypothesis testing, but they are useful for testing the basic properties of our correlation metrics and misalignment estimators. We find that the mock skies produce null results within the realization-dependent scatter.

To assess the noise level in the parity-violating cross-spectra, we consider the half-mission cross-powers (Spearman version of Equation (B2)),

$$XY_{\rm lo}^{(1)} \times XY_{\rm lo}^{(2)} \equiv s_s(D_{\rm lo}^{X^{(1)}Y^{(1)}}, D_{\rm lo}^{X^{(2)}Y^{(2)}}), \quad (39)$$

where $X^{(i)}$ and $Y^{(i)}$ are the X and Y fields, respectively, from the ith half-mission. We form a similar quantity for the high-pass-filtered observables:

$$XY_{\rm hi}^{(1)} \times XY_{\rm hi}^{(2)} \equiv s_s(D_{\rm hi}^{X^{(1)}Y^{(1)}}, D_{\rm hi}^{X^{(2)}Y^{(2)}}). \quad (40)$$

Both $XY_{\rm lo}^{(1)} \times XY_{\rm lo}^{(2)}$ and $XY_{\rm hi}^{(1)} \times XY_{\rm hi}^{(2)}$ are limited only by noise. When noise is subdominant to the sky components, they will show strong positive signals; when noise is significant, they will decay to zero. We plot $XY_{\rm lo}^{(1)} \times XY_{\rm lo}^{(2)}$ and $XY_{\rm hi}^{(1)} \times XY_{\rm hi}^{(2)}$ as red and purple bands, respectively, in Figure 16, where we find that, in general, the high-ℓquantities are substantially noisier than the low-ℓ quantities.

As discussed in Section 7.1, half-mission cross-powers like $\hat{\psi}_{\rm hi}^{(1)} \times \hat{\psi}_{\rm hi}^{(2)}$ and $XY_{\rm hi}^{(1)} \times XY_{\rm hi}^{(2)}$ set rough upper limits on the observable strength of the signals we are seeking. In the case of Figure 16, we must consider the fidelity of both $\hat{\psi}$ (red/purple bands in Figure 12) and XY (red/purple in Figure 16). When $\hat{\psi} \times XY$ is of the same order as the half-mission cross-powers, a nonnegligible fraction of the variation in XY is associated with harmonically coherent misalignment. In Figure 16, this is the case for $E_{\rm H\,I}B_{\rm d}$, $B_{\rm H\,I}E_{\rm d}$, $T_{\rm H\,I}B_{\rm d}$, and $T_{\rm d}B_{\rm d}$. For $E_{\rm d}B_{\rm d}$, the half-mission cross-powers, especially $(E_{\rm d}B_{\rm d})_{\rm hi}^{(1)} \times (E_{\rm d}B_{\rm d})_{\rm hi}^{(2)}$, are too noisy to make a reliable comparison.

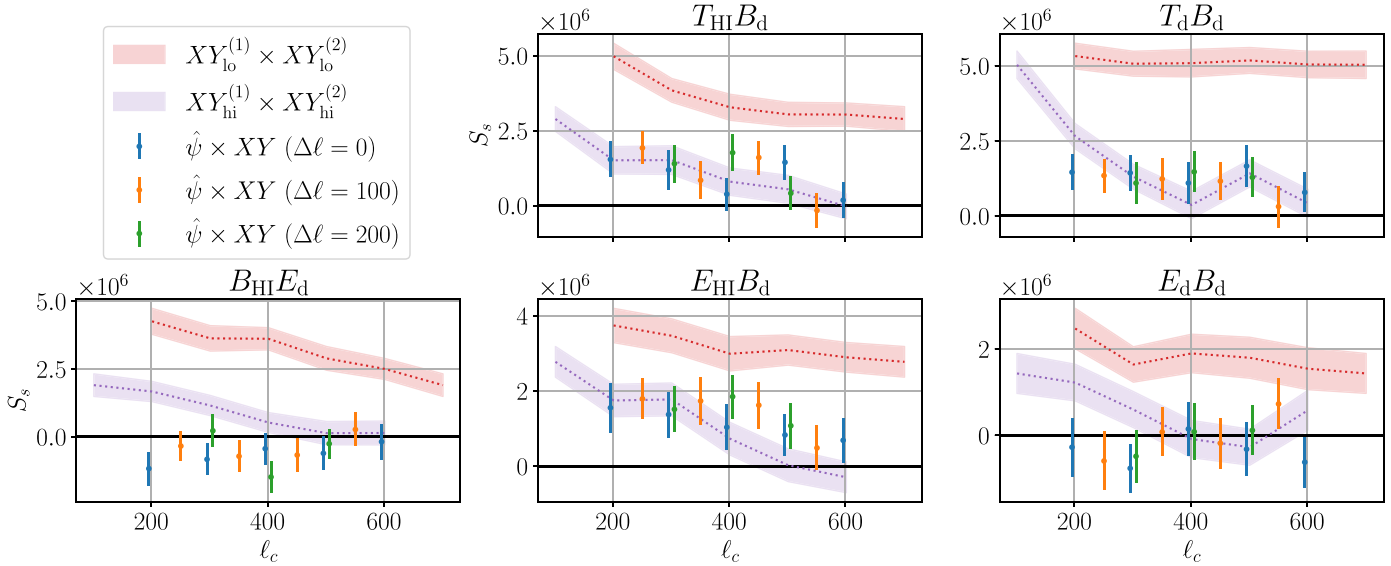

Figure 16. Cross-power S_s between misalignment angle $\hat{\psi}$ and parity-violating cross-spectra XY (e.g., Equation (38)) for patches defined by $N_{\rm side} = 8$ and $f_{\rm sky} = 70\%$. We consider three values for $\Delta\ell$; the data points are offset from ℓ_c for visual purposes. The red and purple bands show, respectively, the low- and high-pass-filtered half-mission cross-powers for the quantity in the subtitle (Equations (39) and (40)). We find the expected correlations with $E_{\rm H\,I}B_{\rm d}$, $B_{\rm H\,I}E_{\rm d}$, $T_{\rm H\,I}B_{\rm d}$, and $T_{\rm d}B_{\rm d}$ (Equations (17)–(19)).

Table 3

Statistical Significance (in Units of σ) of Measurements of the Harmonically Coherent Correlations between $\hat{\psi}$ and $T_{\rm d}B_{\rm d}$ ($E_{\rm d}B_{\rm d}$), e.g., Those Shown in Figure 16, for Different Values of $N_{\rm side}$ (Rows with Side Lengths Provided Parenthetically) and $f_{\rm sky}$ (Columns)

	40%	60%	70%	80%	90%	100%
2 (29.°3)	1.8 (1.4)	2.1 (1.2)	2.2 (1.8)	1.8 (1.9)	2.5 (1.3)	2.6 (1.5)
4 (14.°7)	1.3 (−0.5)	2.5 (0.6)	2.8 (1.3)	3.0 (3.0)	2.3 (2.4)	1.7 (1.2)
8 (7.°3)	1.9 (−0.9)	1.5 (−1.5)	2.9 (−0.8)	3.7 (−0.9)	3.9 (0.8)	4.4 (0.2)

Note. The $\hat{\psi} \times T_{\rm d}B_{\rm d}$ significances are all positive and tend to increase with $N_{\rm side}$ and $f_{\rm sky}$. The $\hat{\psi} \times E_{\rm d}B_{\rm d}$ significances are mostly positive but generally smaller.

We estimate the statistical significance of measurements like those of Figure 16 by following a prescription similar to those of Sections 7.1 and 7.2. The weights used in combining the measurements now account for noise in both $\hat{\psi}$ (bands in Figure 12) and the cross-spectra (bands in Figure 16). For the example of Figure 16, we find that $\hat{\psi} \times T_{\rm d}B_{\rm d}$ has a significance of 2.9σ, while $\hat{\psi} \times E_{\rm d}B_{\rm d}$ yields -0.8σ, i.e., consistency with null. The cross-powers with $T_{\rm H\,I}B_{\rm d}$, $E_{\rm H\,I}B_{\rm d}$, and $B_{\rm H\,I}E_{\rm d}$ yield, respectively, 2.8σ, 2.8σ, and -1.75σ, where the last value is expected to be negative (Equation (18)). Since the Planck–H I cross-spectra are approximate measures of the dust rotation relative to the H I template, the latter correlations can be considered further confirmation of the harmonic coherence of $\hat{\psi}$ (Section 7.1).

In Table 3, we compile estimates of statistical significance for $\hat{\psi} \times T_{\rm d}B_{\rm d}$ and $\hat{\psi} \times E_{\rm d}B_{\rm d}$ using different choices for $N_{\rm side}$ and $f_{\rm sky}$. The estimates are correlated with each other, and we have not attempted to estimate a global significance. What can be gleaned, however, is a tendency for positive correlations with $T_{\rm d}B_{\rm d}$ and mostly insignificant correlations with $E_{\rm d}B_{\rm d}$. A few variations show a significance above 2σ for $E_{\rm d}B_{\rm d}$, and a majority are positive. But the overall picture is less compelling than in the case of $T_{\rm d}B_{\rm d}$. The $(E_{\rm d}B_{\rm d})^{(1)}_{\rm lo} \times (E_{\rm d}B_{\rm d})^{(2)}_{\rm lo}$ and $(E_{\rm d}B_{\rm d})^{(1)}_{\rm hi} \times (E_{\rm d}B_{\rm d})^{(2)}_{\rm hi}$ cross-powers (Equations (39) and (40); shown as red and purple bands in Figure 16) are two to three times smaller than the corresponding $T_{\rm d}B_{\rm d}$ quantities at low $\ell_{\rm c}$ and have fractionally larger uncertainties. Furthermore, the $(E_{\rm d}B_{\rm d})^{(1)}_{\rm hi} \times (E_{\rm d}B_{\rm d})^{(2)}_{\rm hi}$ signal becomes consistent with zero for $\ell_c \gtrsim 300$; i.e., $(E_{\rm d}B_{\rm d})_{\rm hi}$ becomes noise-dominated. Given these considerations, it is consistent with our expectations that the $\sim 3\sigma$ results for $\hat{\psi} \times T_{\rm d}B_{\rm d}$ weaken to mostly null results for $\hat{\psi} \times E_{\rm d}B_{\rm d}$.

The real data, within the limits of the noise, are broadly consistent with our expectations, namely, positive correlations between $\hat{\psi}$ and $T_{\rm d}B_{\rm d}$, $E_{\rm d}B_{\rm d}$, $T_{\rm H\,I}B_{\rm d}$, and $E_{\rm H\,I}B_{\rm d}$ and negative between $\hat{\psi}$ and $B_{\rm H\,I}E_{\rm d}$, though these signals disappear for some choices of $N_{\rm side}$, $\ell_{\rm c}$, and $\Delta\ell$. In particular, the signal tends to decay as $\ell_{\rm c}$ increases, which we expect due to increased noise in the high-pass-filtered quantities. For $N_{\rm side} = 4$, the expected negative correlation with $B_{\rm H\,I}E_{\rm d}$ appears only for $\ell_c \gtrsim 350$ and is fairly weak. For $N_{\rm side} = 8$, the expected correlation with $E_{\rm d}B_{\rm d}$ disappears.

These results build confidence in our picture of harmonically coherent magnetic misalignment. Alternatively, these correlations can be considered necessary implications of the harmonic coherence of $\hat{\psi}$ (Section 7.1) coupled with the expected relationship between $\hat{\psi}$ and the parity-violating cross-spectra (Sections 8.1 and 8.3). With this perspective, the cross-powers in Figure 16 are merely tests for consistency.

We draw special attention to the correlations between $\hat{\psi}$ and $T_{\rm d}B_{\rm d}$, as the positive $T_{\rm d}B_{\rm d}$ measured by Planck has been recently discussed in the literature (Huffenberger et al. 2020; Weiland et al. 2020; Clark et al. 2021; Huang 2022). Although correlations between $\hat{\psi}$ and $E_{\rm d}B_{\rm d}$ yielded only weak results, we

note the positivity of $(E_{\rm d}B_{\rm d})^{(1)}_{\rm lo} \times (E_{\rm d}B_{\rm d})^{(2)}_{\rm lo}$ (Equation (39); shown as the red band in Figure 16), which indicates on-sky variation in $E_{\rm d}B_{\rm d}$ that rises above the noise level. Variation in $E_{\rm d}B_{\rm d}$ may be attributable to sample-variance fluctuations of underlying parity-even statistical processes, but the particular dust realization that we observe is a foreground that must be mitigated for, e.g., measurements of the CMB. Spatial variation in $E_{\rm d}B_{\rm d}$ may be of relevance for measurements of cosmic birefringence (Minami et al. 2019; Minami & Komatsu 2020; Diego-Palazuelos et al. 2022; Eskilt & Komatsu 2022). If future measurements can more confidently establish a relationship between $\hat{\psi}$ and $E_{\rm d}B_{\rm d}$, foreground removal could be performed more robustly by, e.g., relating $E_{\rm d}B_{\rm d}$ to $T_{\rm d}B_{\rm d}$ and other observables (e.g., Equations (17)–(20)).

9. Conclusion and Outlook

We have extended the work of Clark et al. (2021) in establishing a connection between dust *TB* correlations and the magnetic misalignment of interstellar dust filaments. We have introduced a new version of a Hessian-based H I polarization template, which correlates more strongly with dust *B* modes than the RHT-based template used previously (Section 3). We introduced several spectrum-based misalignment estimators formed from the auto- and cross-spectra of Planck dust maps and H I polarization templates (Section 4.2), and we also introduced a map-based estimator for the misalignment angle (Section 6). We have presented maps of the misalignment angle (Section 6.1) that show a tendency to positive values and a visual correlation with the dust polarization fraction. We have provided evidence for the scale independence (harmonic coherence) of the misalignment angle for multipoles $\ell \lesssim 700$ (Sections 6.5 and 7.1) and for spatial coherence on angular scales of $\sim 1^\circ$ (Section 7.2). On large sky areas at high Galactic latitudes, we find a scale-independent misalignment angle of $\sim 2^\circ$, which is robust to a variety of masking choices (Section 6.7). We have described a set of mock skies (Section 5) containing H I-based filamentary structure, as well as Gaussian-random components, and we have used these mock skies to refine our notion of magnetic misalignment. In particular, we have explored the question of whether the measured misalignment between H I filaments and the magnetic-field orientation is consistent with random fluctuations in the polarization field (Section 8.1). This question motivated a search for scale independence (harmonic coherence) as a salient physical property of magnetic misalignment. We find evidence for a scale-independent correlation between misalignment angle and dust *TB* (Section 8.4). With the noisier *EB*, we find a correlation for some but not all of our masking choices. We also find that the observed positive dust *TB* may be due to a few regions with strong positive misalignment, while the rest of the sky largely respects parity (Section 8.2).

In general, the picture that is beginning to emerge contains the following features.

1. On large scales at high Galactic latitudes, there is a global tendency toward an aggregate misalignment of $\sim 2^\circ$ (Sections 6.5–6.7).
2. Magnetic misalignment is a reliable predictor of parity violation in the dust polarization (Sections 8.2 and 8.3).
3. Magnetic misalignment is partially scale-independent (harmonically coherent; Sections 7.1 and 8.4).

We now provide suggestions for potential improvements to our analysis.

1. The ansatz (Section 4) could be modified to allow for only a fraction of the dust to participate in misalignment. In this work, it is assumed that all of the dust is misaligned, but this may dilute the sensitivity of our estimators. In Clark et al. (2021), this type of concern was addressed in estimating the misalignment-induced *EB* in Equation (12).
2. The H I template (Section 3) could be improved to correlate more strongly with the Planck dust maps. In this work, we introduced a new Hessian-based template, which correlates more strongly with the dust *B* modes than the RHT-based template used in Clark et al. (2021), but the correlation is still less than 20% for $\ell \gtrsim 200$. While the H I-based filamentary model may be fundamentally limited due to diffuse nonfilamentary dust or other dust morphologies, we consider it more likely that a dedicated exploration will yield stronger correlations with the measured dust polarization (G. Halal et al. 2022, in preparation). Magnetic misalignment is a perturbation to the filamentary model, so an increased correlation would improve the sensitivity of all of the H I-related estimators presented in this work.
3. More realistic mock skies or simulations (Section 5) will aid in the physical interpretation of our estimators. For example, the MHD simulations of Kim & Ostriker (2017), which can be converted to the dust polarization maps (Kim et al. 2019) that were considered in Clark et al. (2021), model the solar neighborhood and are publicly available at a resolution of $N_{\rm side} = 128$. Similar simulations with higher resolution and synthetic H I observations could be analyzed with our estimators. Misalignment could also be investigated in synthetic dust polarization observations directly by searching for, e.g., scale independence in *TB* and *EB*. In Section 4 of Clark et al. (2021), this type of analysis was performed on a limited multipole range ($60 < \ell < 120$). Higher-resolution simulations will enable an extension to higher multipoles and further investigation of the link to underlying physics.
4. The pixels weights $w(\hat{\boldsymbol{n}})$ (Section 6) that enter the calculation of $\hat{\psi}$ are likely suboptimal. We checked that our choice reduces variance relative to a uniform weighting, but we have not explored the full space of possibilities. A better choice may be a Wiener filter that prevents a few bright pixels from dominating. Similarly, the correlation metrics used in Sections 7 and 8 could be defined with weights to suppress noisy regions of sky.
5. The large-scale (low-ℓ) misalignment should be considered more rigorously because dust polarization is dominated by these modes. We have mostly limited our investigation to $\ell \gtrsim 100$ to avoid large-scale covariances. But there appears to be a strong positive misalignment on large scales (Figure 7), and we speculate that this may be related to the magnetic-field structure in the vicinity of the Local Bubble (e.g., Lallement et al. 2003; Alves et al. 2018; Leike et al. 2020; Pelgrims et al. 2020; Vergely et al. 2022).
6. Other sources of parity violation should be considered, since magnetic misalignment alone may be insufficient to account for, e.g., the observed *TB*. We mention in

Appendix A.3 that the distribution of dust filaments may itself display a chiral asymmetry even in the limit of perfect magnetic alignment. Both the Hessian- and RHT-based H I templates, which assume perfect alignment, predict a rise in EB for $\ell \lesssim 100$ (Figure 18), though the expected signal is below the Planck noise levels. We defer the investigation of this morphological parity violation to future work.

7. Other magnetic-field tracers, such as starlight polarization and Faraday rotation, could be incorporated to better understand the three-dimensional manifestation of magnetic misalignment. With stellar distance measurements from, e.g., Gaia (Gaia Collaboration et al. 2016), starlight polarization measurements can enable a tomographic reconstruction of Galactic magnetic fields, though this technique is sensitive only to the POS component (Panopoulou et al. 2019). Faraday rotation measures probe the line-of-sight magnetic-field component (Hutschenreuter & Enßlin 2020) and can be combined with model expectations or POS observations to constrain the three-dimensional magnetic-field structure (e.g., Tahani et al. 2019, 2022).

Our misalignment analysis can be applied to a variety of ISM environments. As a method of studying the relative orientations of magnetic fields (not necessarily with dust polarization) and density structures (not necessarily with H I), our approach is complementary to those of, e.g., Planck Collaboration et al. (2016a), Soler et al. (2017), and Fissel et al. (2019), which consider both the diffuse ISM and molecular clouds.

The study of parity violation in Galactic dust polarization is of central importance both for cosmology and for ISM physics. Our investigation has been limited by noise in the Planck polarization maps, and we therefore recommend follow-up surveys at millimeter and submillimeter wavelengths covering large sky fractions with resolution similar to or finer than the HI4PI beamwidth (16.′2). More sensitive measurements will become available from upcoming projects, including the space-based LiteBIRD (Hazumi et al. 2020) and the ground-based Simons Observatory (Hensley et al. 2022), CCAT-prime (CCAT-Prime Collaboration et al. 2023), and CMB Stage 4 (Abazajian et al. 2019).

We thank Dominic Beck, Federico Bianchini, Chao-Lin Kuo, Enrique Lopez-Rodriguez, and Kimmy Wu for advice and helpful conversations. This work was partly supported by the National Science Foundation under grant No. 2106607. Some of the computing was performed on the Sherlock cluster; we thank Stanford University and the Stanford Research Computing Center. This work makes use of observations obtained with Planck (http://www.esa.int/Planck), an ESA science mission with instruments and contributions directly funded by ESA Member States, NASA, and Canada. HI4PI is based on observations with the 100 m telescope of the MPIfR at Effelsberg and the Parkes Radio Telescope, part of the Australia Telescope National Facility, which is funded by the Australian Government and managed by CSIRO.

Software: `healpy` (Zonca et al. 2019), `matplotlib` (Hunter 2007), `NaMaster` (Alonso et al. 2019), `numpy` (Harris et al. 2020), `scipy` (Virtanen et al. 2020).

Appendix A
Hessian Method: Supplemental Material

Here we provide additional information related to the Hessian method (Section 3) that supports some of the analysis choices made in this work. In the comparisons below, we will occasionally use the subscript "H" to refer to the Hessian method and "RHT" for the rolling Hough transform. With the subscript "H I," we implicitly refer to the Hessian method as in the main text.

A.1. Comparison with the RHT

The RHT is another filament-finding algorithm (Clark et al. 2014) from which we can produce polarization templates that correlate strongly with the dust polarization measured by Planck (Clark et al. 2015; Clark & Hensley 2019).

We find that the Hessian correlates more strongly with the Planck dust B modes than the RHT for $\ell \gtrsim 100$, and we show a comparison in Figure 17. In the E modes, the two perform similarly. In these comparisons, the RHT is constructed from velocities spanning -90 to 90 km s^{-1} (as in Clark & Hensley 2019), while the Hessian template is constructed from the restricted range of -15 to 4 km s^{-1}, (Section 3.1).

For the T template, we consider two choices for the RHT. One might use $I_{\rm HI4PI}$, i.e., the HI4PI intensity map (HI4PI Collaboration et al. 2016) without any processing. Since we are especially interested in the filamentary component of the dust intensity, it may be preferable to high pass filter the HI4PI intensity as in the first step in the RHT algorithm of Clark & Hensley (2019). The filter is implemented as an unsharp mask with FWHM $= 30'$. Denote the high-pass-filtered intensity by $T_{\rm RHT}$. In Figure 17, we find that $I_{\rm HI4PI}$ correlates more strongly than $T_{\rm RHT}$ with the Planck T modes. This is not necessarily the relevant metric, however, since we are specifically targeting filaments. We also present in Figure 17 the correlation with the Planck E modes, since the TE correlation is a signature of filamentary polarization. We find that $r_\ell^{T_{\rm RHT}E_{\rm d}}$ is generally larger than $r_\ell^{I_{\rm H\,I4PI}E_{\rm d}}$. For this reason, we prefer $T_{\rm RHT}$ as a template for filamentary dust intensity.

The Hessian intensity T_H (Equations (11) and (14)) is defined mainly by the Hessian eigenvalues. In Figure 17, we find that $r_\ell^{T_H T_{\rm d}}$ is smaller than $r_\ell^{T_{\rm RHT}T_{\rm d}}$ but that $r_\ell^{T_H E_{\rm d}}$ is similar to and, at high ℓ, slightly larger than $r_\ell^{T_{\rm RHT}E_{\rm d}}$.

On account of the greater correlation in the B modes, we have selected the Hessian-based template as our baseline. The T templates considered above all correlate strongly with both $T_{\rm d}$ and $E_{\rm d}$ and at roughly the same level. The E templates for both algorithms correlate with $E_{\rm d}$ at roughly the same level.

We defer to future work a more detailed investigation of these and related filament-finding algorithms for the construction of polarization templates (G. Halal et al. 2022, in preparation). Each can be modified and tuned by making different choices for, e.g., velocity binning, weighting, spatial filtering, etc.

A.2. Transfer Function

The H I-based polarization templates have different mode structures than the Planck dust maps. For example, the Hessian method upweights small-scale features; the E_H and B_H power spectra increase with ℓ. The RHT also upweights small-scale features but especially emphasizes the multipole range $300 \lesssim \ell$

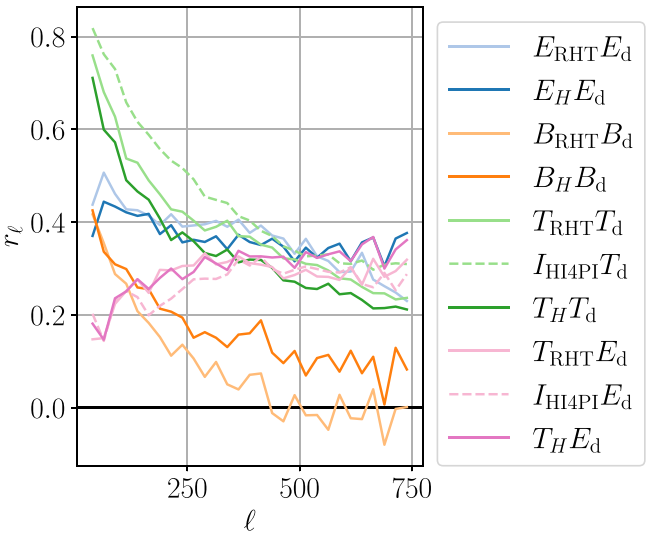

Figure 17. Correlation r_ℓ between Planck dust maps (d) and the RHT, the Hessian method (H), and the raw HI4PI intensity map ($I_{\rm HI4PI}$) with multipole bin width $\Delta\ell = 25$ on a 70% Galaxy mask.

$\lesssim 500$ for $E_{\rm RHT}$ and $150 \lesssim \ell \lesssim 350$ for $B_{\rm RHT}$ (with RHT parameters set to those of Clark & Hensley 2019).

Correlations, e.g., those presented in Clark & Hensley (2019), are insensitive to differences in mode structure because they are evaluated in individual multipole bins. The upweighting of one multipole bin relative to another is normalized out of the calculation. The difference in mode structure can be viewed as a multipole-dependent transfer function.

For the purposes of converting our H I-based polarization templates into quantities that are directly comparable to the Planck dust maps, we assume a transfer function that depends only on multipole ℓ:

$$k_\ell^{(X)} \equiv \frac{D_\ell^{X_{\rm H\,I} X_{\rm d}}}{D_\ell^{X_{\rm H\,I} X_{\rm H\,I}}}. \tag{A1}$$

This transfer function converts an H I-based quantity into dust-intensity units with a mode structure that is directly comparable to the observed dust field. We find that $k_\ell(X)$ rises strongly at low multipoles, which is an indication that the H I templates tend to underpredict the amplitude of large-scale dust polarization relative to small-scale. In spite of this underprediction, the correlations, which normalize out the ℓ dependence, are actually stronger at low ℓ.

There is no guarantee that the transfer function $k_\ell^{(X)}$ provides a representative estimate of the amplitude of the H I-based modes in the real dust maps. The amplitudes may depend on both ℓ and m, the spherical-harmonic eigenvalues. We use $k_\ell^{(X)}$ as a rough conversion factor to make direct comparisons between the H I templates and the real dust maps.

Because the Hessian-based template correlates nonvanishingly with Planck up to at least $\ell = 750$, the transfer function remains usable across the entire multipole range considered in our analysis.

A.3. Parity in the Templates

The H I templates are produced under the assumption of perfect magnetic alignment. Even so, chirality in the filament morphology could produce parity-violating signatures such as nonzero $T_{\rm H\,I}B_{\rm H\,I}$ and $E_{\rm H\,I}B_{\rm H\,I}$.

We computed these parity-violating cross-spectra for both the Hessian and the RHT templates.[8] To determine if the results are significant, we compare to the $T_{\rm d}B_{\rm d}$ and $E_{\rm d}B_{\rm d}$ spectra from the Planck dust maps. To make this comparison, we applied the transfer function $k_\ell^{(X)}$ introduced in Appendix A.2, which converts the H I templates into dust-intensity units. The results are shown in Figure 18.

The Planck $T_{\rm d}B_{\rm d}$ displays a positive signal, and $T_{\rm H\,I}B_{\rm H\,I}$ is negligible in comparison. The Planck $E_{\rm d}B_{\rm d}$ appears to be consistent with noise, and we find that $E_{\rm H\,I}B_{\rm H\,I}$ is negligible in comparison with the fluctuations. The above comparisons are restricted to $\ell > 100$, which is the target multipole range of the analysis presented in this work.

Based on these observations, the intrinsic (or morphological) H I-based $T_{\rm H\,I}B_{\rm H\,I}$ and $E_{\rm H\,I}B_{\rm H\,I}$ are assumed to vanish in our analysis.

Intriguingly, however, the H I-based $E_{\rm H\,I}B_{\rm H\,I}$ shows a rise for $\ell < 150$. With finer multipole binning $\Delta\ell$, we find that this rise persists down to $\ell = 17$ with $\Delta\ell = 10$, the lowest bin center with the finest binning that we checked. There is a corresponding rise in $T_{\rm H\,I}B_{\rm H\,I}$ that persists down to $\ell = 27$. In all cases, the H I-based predictions are subdominant to the expected noise in the Planck measurements but only by a factor of $\sim$10. We defer to future work an investigation of these low-ℓ H I-based predictions, which could represent a source of parity violation independent of magnetic misalignment.

Appendix B
Cross-power and Correlation Metrics

We make use of a variety of correlation metrics. We wish for these metrics to be numerically stable, unbiased by noise or other covariances, and, in some cases, sensitive to two different effects simultaneously.

Let $\overline{X}$ be the sample mean for a set of n measurements $\{X_i\}$. The mean-subtracted observable is

$$x_i \equiv X_i - \overline{X}. \tag{B1}$$

The index i will be labeling the central sky coordinate of small patches. Unless the sky mask has been chosen to retain relatively isotropic dust power, the dust intensity can vary dramatically across the observing region. It is therefore likely that the set of observables $\{x_i\}$ is dominated by the brightest patches. Because many of the quantities of interest range over several orders of magnitude, we prefer metrics related to the Spearman rank correlation coefficient for which the observables are converted to rank variables. This avoids overweighting bright sight lines. By collapsing the observables onto ranks, the absolute magnitudes are less important, and both large and small values of X contribute equally.

We consider correlation metrics for two data vectors X and Y. When the data vectors are noisy, it is more useful to consider a cross-power, which is essentially the numerator of a Pearson correlation coefficient. We define the Pearson cross-power of X

[8] Our RHT implementation has been updated since Clark & Hensley (2019). We call this new version the "spherical RHT" because it employs a convolution on the sphere. This both speeds up the computation and removes a spurious $E_{\rm RHT}B_{\rm RHT}$ correlation that is present at the 5% level in the H I templates of Clark & Hensley (2019). We will report on the spherical RHT in greater detail in future work (G. Halal et al. 2022, in preparation).

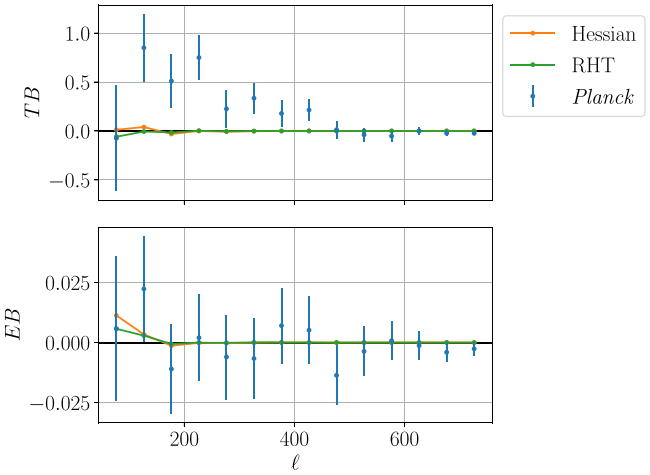

Figure 18. Parity-violating *TB* (top) and *EB* (bottom) spectra measured by Planck (blue) and predicted by the Hessian H I template (orange) and the RHT (green). The multipole bin width is $\Delta\ell = 50$. The units are μK_{RJ}^2. The error bars are derived from Gaussian variances. The H I-based predictions include the transfer function of Appendix A.2. For $\ell > 100$, the multipole range used in most of our analysis, the H I-based predictions are negligible in comparison with the Planck measurements.

and Y as

$$s_p(X, Y) \equiv \sum_i x_i y_i. \tag{B2}$$

As mentioned above, we will often prefer quantities related to the Spearman rank correlation coefficient. For the Spearman cross-power, which we denote $s_s(X, Y)$, we simply convert x_i and y_i to rank variables in Equation (B2).

Both Pearson and Spearman correlation coefficients are biased low by noise. We can use data splits to avoid positive-definite quantities like x_i^2. For data split $j \in \{1, 2\}$, define the mean-subtracted observable as $x_i^{(j)} \equiv X_i^{(j)} - \overline{X}$; i.e., the mean that is subtracted is from the full data. We modify the denominator of the Pearson correlation coefficient to include data-split cross-powers (Equation (B2)), which are unbiased by noise,

$$\tilde{r}_p(X, Y) \equiv \frac{s_p(X, Y)}{\sqrt{|s_p(X^{(1)}, X^{(2)})||s_p(Y^{(1)}, Y^{(2)})|}}, \tag{B3}$$

where the tilde serves to indicate that this is a modification to the conventional definition of a Pearson correlation coefficient. To avoid numerical pathologies in the case of noisy data, we have taken the absolute values of the cross-powers in the denominator. When noise-dominated, $\tilde{r}_p(X, Y)$ can return values larger in magnitude than unity. In such cases, we will typically avoid correlation coefficients (Equation (B3)) in favor of cross-powers (Equation (B2)). We can form a Spearman version of Equation (B3), which we denote $\tilde{r}_s(X, Y)$, by using s_s (Spearman version of Equation (B2)) in place of s_p.

While $\tilde{r}_p(X, Y)$ (Equation (B3)) avoids a suppression due to noise biases, it may still be vulnerable to noise covariances between X and Y, though this is only a concern if X and Y are drawn from related data sets. For instance, both may be derived from Planck dust maps, so noise covariances must be considered seriously. We define the half-mission cross-correlation coefficient

$$\tilde{r}_p^{(\mathrm{HM})}(X, Y) \equiv \frac{s_p(X^{(1)}, Y^{(2)}) + s_p(X^{(2)}, Y^{(1)})}{2\sqrt{|s_p(X^{(1)}, X^{(2)})||s_p(Y^{(1)}, Y^{(2)})|}}, \tag{B4}$$

which measures a simultaneous correlation between opposite data splits of X and Y. The convenient splits for Planck are half-mission maps. As above, we form the Spearman version simply by using s_s in place of s_p.

In some cases, we will wish to measure simultaneous correlations between two pairs of observables, e.g., a correlation between W and X and a correlation between Y and Z. We define the four-variable cross-power

$$S_p(W, X, Y, Z) \equiv \sum_i (w_i x_i + y_i z_i). \tag{B5}$$

As above, we can construct a Spearman version of this cross-power, which we denote $S_s(W, X, Y, Z)$, by converting to rank variables.

B.1. Statistical Inference

For statistical inference regarding our correlation metrics, we use permutation tests. For two-variable metrics, we randomly permute Y to obtain $\pi(Y)$, where the function π defines a random permutation that here acts on the data vector Y. We then compute, e.g., $s_s(X, \pi(Y))$. With a large number of permutations, we can build a null-hypothesis distribution for $s_s(X, Y)$. Similar permutation tests can be formed for the other two-variable correlation metrics. In this work, each ensemble of permutations contains 200 realizations. Our results change only negligibly with larger permutation ensembles.

For the four-variable correlation metrics, we also appeal to permutation tests, but we coordinate the permutations of X and Z. We form many realizations of, e.g., $S_s(W, \pi(X), Y, \pi(Z))$.

We will often estimate uncertainties on our correlation coefficients by converting to z scores and taking half the difference between the value at 1σ and the value at -1σ. For $s_s(X, Y)$, call this uncertainty estimate $\sigma[s_s(X, Y)]$, and we maintain similar notational conventions for the other correlation metrics.

ORCID iDs

Ari J. Cukierman https://orcid.org/0000-0002-7471-719X
S. E. Clark https://orcid.org/0000-0002-7633-3376
George Halal https://orcid.org/0000-0003-2221-3018

References

Abazajian, K., Addison, G., Adshead, P., et al. 2019, arXiv:1907.04473
Abitbol, M. H., Hill, J. C., & Johnson, B. R. 2016, MNRAS, 457, 1796
Ade, P. A. R., Arnold, K., Atlas, M., et al. 2015, PhRvD, 92, 123509
Alonso, D., Sanchez, J., Slosar, A. & LSST Dark Energy Science Collaboration 2019, MNRAS, 484, 4127
Alves, M. I. R., Boulanger, F., Ferriere, K., & Montier, L. 2018, A&A, 611, L5
Arzoumanian, D., Andre, P., Didelon, P., et al. 2011, A&A, 529, L6
Bennett, C. L., Larson, D., Weiland, J. L., et al. 2013, ApJS, 208, 20
Berdyugin, A., Piirola, V., & Teerikorpi, P. 2004, A&A, 424, 873
Berdyugin, A., & Teerikorpi, P. 2002, A&A, 384, 1050
Berdyugin, A., Teerikorpi, P., Haikala, L., et al. 2001, A&A, 372, 276
Bianchini, F., Wu, W. L. K., Ade, P. A. R., et al. 2020, PhRvD, 102, 083504
BICEP2 Collaboration,Keck Array Collaboration, Ade, P. A. R., et al. 2017, PhRvD, 96, 102003
BICEP/Keck, Ade, P. A. R., Ahmed, Z., et al. 2021, PhRvD, 103, 042002
BICEP/Keck, Ade, P. A. R., Ahmed, Z., et al. 2022, PhRvD, 105, 022006
Blackman, E. G. 2015, SSRv, 188, 59

Bracco, A., Candelaresi, S., Del Sordo, F., & Brandenburg, A. 2019, A&A, 621, A97
Brandenburg, A., & Subramanian, K. 2005, PhR, 417, 1
Caldwell, R. R., Hirata, C., & Kamionkowski, M. 2017, ApJ, 839, 91
Carroll, S. M. 1998, PhRvL, 81, 3067
Carroll, S. M., Field, G. B., & Jackiw, R. 1990, PhRvD, 41, 1231
CCAT-Prime collaboration, Aravena, M., Austermann, J. E., et al. 2023, ApJS, 264, 7
Choi, S. K., Hasselfield, M., Ho, h. P., et al. 2020, JCAP, 2020, 045
Clark, S. E., & Hensley, B. S. 2019, ApJ, 887, 136
Clark, S. E., Hill, J. C., Peek, J. E. G., Putman, M. E., & Babler, B. L. 2015, PhRvL, 115, 241302
Clark, S. E., Kim, C.-G., Hill, J. C., & Hensley, B. S. 2021, ApJ, 919, 53
Clark, S. E., Peek, J. E. G., & Putman, M. E. 2014, ApJ, 789, 82
Colombi, S., Pogosyan, D., & Souradeep, T. 2000, PhRvL, 85, 5515
Diego-Palazuelos, P., Eskilt, J. R., Minami, Y., et al. 2022, PhRvL, 128, 091302
Eskilt, J. R., & Komatsu, E. 2022, PhRvD, 106, 063503
Feng, B., Li, H., Li, M., & Zhang, X. 2005, PhLB, 620, 27
Feng, B., Li, M., Xia, J.-Q., Chen, X., & Zhang, X. 2006, PhRvL, 96, 221302
Ferguson, K. R., Anderson, A. J., Whitehorn, N., et al. 2022, PhRvD, 106, 042011
Fissel, L. M., Ade, P. A. R., Angile, F. E., et al. 2019, ApJ, 878, 110
Forero-Romero, J. E., Hoffman, Y., Gottlober, S., Klypin, A., & Yepes, G. 2009, MNRAS, 396, 1815
Gaia Collaboration, Prusti, T., de Bruijne, J. H. J., et al. 2016, A&A, 595, A1
Górski, K. M., Hivon, E., Banday, A. J., et al. 2005, ApJ, 622, 759
Grain, J., Tristram, M., & Stompor, R. 2009, PhRvD, 79, 123515
Gruppuso, A., Gerbino, M., Natoli, P., et al. 2016, JCAP, 2016, 001
Hacar, A., Clark, S., Heitsch, F., et al. 2022, arXiv:2203.09562
Harari, D., & Sikivie, P. 1992, PhLB, 289, 67
Harris, C. R., Millman, K. J., van der Walt, S. J., et al. 2020, Natur, 585, 357
Hazumi, M., Ade, P. A. R., Adler, A., et al. 2020, Proc. SPIE, 11443, 114432F
Heiles, C. 2000, AJ, 119, 923
Hensley, B. S., Zhang, C., & Bock, J. J. 2019, ApJ, 887, 159
Hensley, B. S., Clark, S. E., Fanfani, V., et al. 2022, ApJ, 929, 166
Hervias-Caimapo, C., & Huffenberger, K. M. 2022, ApJ, 928, 65
HI4PI Collaboration, Ben Bekhti, N., Flöer, L., et al. 2016, A&A, 594, A116
Hildebrand, R. H. 1988, QJRAS, 29, 327
Huang, Z. 2022, Univ, 8, 423
Huffenberger, K. M., Rotti, A., & Collins, D. C. 2020, ApJ, 899, 31
Hunter, J. D. 2007, CSE, 9, 90
Hutschenreuter, S., & Enßlin, T. A. 2020, A&A, 633, A150
Iverson, K. E. 1962, A Programming Language (John Wiley & Sons, Inc.: New York, NY, USA)
Jow, D. L., Hill, R., Scott, D., et al. 2017, MNRAS, 474, 1018
Kalberla, P. M. W., Kerp, J., & Haud, U. 2021, A&A, 654, A91
Kalberla, P. M. W., Kerp, J., Haud, U., et al. 2016, ApJ, 821, 117
Kamionkowski, M., Kosowsky, A., & Stebbins, A. 1997, PhRvL, 78, 2058
Kandel, D., Lazarian, A., & Pogosyan, D. 2017, MNRAS, 472, L10
Kaufman, J. P., Miller, N. J., Shimon, M., et al. 2014, PhRvD, 89, 062006
Keating, B. G., Shimon, M., & Yadav, A. P. S. 2013, ApJL, 762, L23
Kim, C.-G., Choi, S. K., & Flauger, R. 2019, ApJ, 880, 106
Kim, C.-G., & Ostriker, E. C. 2017, ApJ, 846, 133
Knuth, D. E. 1992, Amer. Math. Monthly, 99, 403
Kritsuk, A. G., Flauger, R., & Ustyugov, S. D. 2018, PhRv, 121, 021104
Lallement, R., Welsh, B. Y., Vergely, J. L., Crifo, F., & Sfeir, D. 2003, A&A, 411, 447
Leike, R. H., Glatzle, M., & Enßlin, T. A. 2020, A&A, 639, A138
Lenz, D., Hensley, B. S., & Dore, O. 2017, ApJ, 846, 38
Liu, G.-C., Lee, S., & Ng, K.-W. 2006, PhRvL, 97, 161303
Lue, A., Wang, L., & Kamionkowski, M. 1999, PhRvL, 83, 1506
Marsh, D. J. E. 2016, PhR, 643, 1
Martin, P. G. 2007, EAS, 23, 165
Martin, P. G., Blagrave, K. P. M., Lockman, F. J., et al. 2015, ApJ, 809, 153
McClure-Griffiths, N. M., Dickey, J. M., Gaensler, B. M., Green, A. J., & Haverkorn, M. 2006, ApJ, 652, 1339
McClure-Griffiths, N. M., Pisano, D. J., Calabretta, M. R., et al. 2009, ApJS, 181, 398
Men'shchikov, A. 2013, A&A, 560, A63
Minami, Y., & Komatsu, E. 2020, PhRvL, 125, 221301
Minami, Y., Ochi, H., Ichiki, K., et al. 2019, PTEP, 2019, 083E02
Namikawa, T., Guan, Y., Darwish, O., et al. 2020, PhRv, 101, 083527
Page, L., Hinshaw, G., Komatsu, E., et al. 2007, ApJS, 170, 335
Panopoulou, G. V., Tassis, K., Skalidis, R., et al. 2019, ApJ, 872, 56
Peek, J. E. G., Babler, B. L., Zheng, Y., et al. 2018, ApJS, 234, 2
Pelgrims, V., Ferriere, K., Boulanger, F., Lallement, R., & Montier, L. 2020, A&A, 636, A17
Planck Collaboration, Adam, R., Ade, P. A. R., et al. 2016a, A&A, 586, A135
Planck Collaboration, Ade, P. A. R., Aghanim, N., et al. 2016b, A&A, 586, A141
Planck Collaboration, Adam, R., Ade, P. A. R., et al. 2016c, A&A, 586, A133
Planck Collaboration, Aghanim, N., Ashdown, M., et al. 2016d, A&A, 596, A110
Planck Collaboration, Akrami, Y., Ashdown, M., et al. 2020a, A&A, 641, A11
Planck Collaboration, Aghanim, N., Akrami, Y., et al. 2020b, A&A, 641, A3
Planck Collaboration, Akrami, Y., Andersen, K. J., et al. 2020c, A&A, 643, A42
Planck Collaboration, Akrami, Y., Ashdown, M., et al. 2020d, A&A, 641, A4
Planck Collaboration, Aghanim, N., Akrami, Y., et al. 2020e, A&A, 641, A12
Polychroni, D., Schisano, E., Elia, D., et al. 2013, ApJL, 777, L33
Seljak, U., & Zaldarriaga, M. 1997, PhRvL, 78, 2054
Soler, J. D., Ade, P. A. R., Angile, F. E., et al. 2017, A&A, 603, A64
Sousbie, T. 2011, MNRAS, 414, 350
Stein, W. 1966, ApJ, 144, 318
Tahani, M., Plume, R., Brown, J. C., Soler, J. D., & Kainulainen, J. 2019, A&A, 632, A68
Tahani, M., Lupypciw, W., Glover, J., et al. 2022, A&A, 660, A97
Vergely, J. L., Lallement, R., & Cox, N. L. J. 2022, A&A, 664, A174
Virtanen, P., Gommers, R., Oliphant, T. E., et al. 2020, NatMe, 17, 261
Weiland, J. L., Addison, G. E., Bennett, C. L., Halpern, M., & Hinshaw, G. 2020, ApJ, 893, 119
Winkel, B., Kerp, J., Floer, L., et al. 2016, A&A, 585, A41
Yadav, A. P. S., Su, M., & Zaldarriaga, M. 2010, PhRvD, 81, 063512
Zaldarriaga, M. 2001, PhRvD, 64, 103001
Zonca, A., Singer, L., Lenz, D., et al. 2019, JOSS, 4, 1298